The Electrochemical Society
Advancing solid state & electrochemical science & technology

OPEN ACCESS

Review—Supercritical Deposition: A Powerful Technique for Synthesis of Functional Materials for Electrochemical Energy Conversion and Storage

View the article online for updates and enhancements.

Review—Supercritical Deposition: A Powerful Technique for Synthesis of Functional Materials for Electrochemical Energy Conversion and Storage

Sansim Bengisu Barim,[1] **Erdal Uzunlar,**[2] **Selmi Erim Bozbag,**[1] **and Can Erkey**[1,3,z]

[1]*Department of Chemical and Biological Engineering, Koç University, Istanbul, Turkey*
[2]*Department of Chemical Engineering, İzmir Institute of Technology, 35430 İzmir, Turkey*
[3]*Koç University Tüpraş Energy Center, Koç University, Istanbul, Turkey*

Supercritical fluid-based technologies are increasingly being used to develop novel functional nanostructured materials or improve the properties of existing ones. Among these, supercritical deposition (SCD) is an emerging technique to incorporate metals on supports. It has been used to deposit a wide variety of single or multi-metallic morphologies such as highly dispersed species, nanoparticles, nanorods and conformal films on high surface area supports, polymers and crystalline substrates. SCD is also attracting increasing attention for preparation of micro or nano-architectured functional materials in a highly controllable manner for electrochemical energy conversion and storage systems. Increasing number of studies in the literature demonstrates that materials synthesized using SCD are comparable or superior in performance as compared to their conventional counterparts. In this review, an overview of the fundamentals of the SCD technique is presented. Properties of a wide variety of nanostructured functional materials such as supported nanoparticles and films prepared using SCD for electrochemical applications are summarized. The electrochemical performance of these materials in electrochemical tests and also in fuel cells, electrolyzers and Li-ion batteries are also presented.

The advantages of supercritical fluids (SCFs) over other solvents or media are primarily due to their physicochemical properties, which are intermediate between a gas and a liquid and are easily adjustable with changes in temperature and pressure. The P–T diagram of a pure compound is given in Fig. 1. The liquid–gas co-existence curve terminates at the critical point, the coordinates of which are the critical temperature (T_c) and critical pressure (P_c). A SCF is a fluid that has been compressed and heated above its T_c and P_c. At typical processing conditions, SCFs possess interesting properties such as liquid-like density, gas-like viscosity, and the diffusion coefficients in SCFs are higher than in liquids. The typical values of thermophysical properties of the gas, liquid, and the supercritical state are given in Table I.

Supercritical carbon dioxide (scCO$_2$) is preferred over other SCFs due to its relatively easily accessible T_c (31.2 °C) and P_c (7.38 MPa). These mild supercritical conditions make CO$_2$ an attractive medium for a variety of applications especially for processing of thermally labile compounds. scCO$_2$ also has other remarkable advantages such as being abundant, inexpensive, non-flammable, non-toxic, and environmentally benign. Furthermore, like all the other SCFs, mass transfer rates in scCO$_2$ are considerably faster than that of the liquid solvents and scCO$_2$ can penetrate easily to the depths of the highly porous nanostructures. The solvating power of scCO$_2$ is a function of its density which increases with pressure at constant temperature. For example, at constant temperature, the solubility of a solute in scCO$_2$ increases with pressure significantly near the P_c and then continues to increase monotonically. The solubility of a solute in scCO$_2$ increases or decreases with increasing temperature depending on the pressure. This behavior occurs due to the compensation of the decline of CO$_2$'s solvating power due to decreasing density by the increase in solvating power due to the increase of the vapor pressure of the solute with increasing temperature. The solubility of a solute in scCO$_2$ is significantly higher than predicted assuming that the solute and scCO$_2$ forms an ideal gas mixture. This is primarily due to the non-ideal behavior of the mixture as the density of scCO$_2$ approaches liquid like densities.

Non-polar compounds have usually high solubility in scCO$_2$ due to the fact that CO$_2$ is a non-polar solvent. However, polar molecules can also be dissolved in scCO$_2$ to a certain extent since scCO$_2$ has a large quadrupole moment. The solvating power of scCO$_2$ can be increased by the addition of modifiers or co-solvents such as ethanol, methanol, and hexane at concentrations ranging from 1 to 20 wt.%.

scCO$_2$ is completely miscible with gases such as H$_2$, O$_2$, or CO at temperatures above 31.2 °C whereas gases are only sparingly soluble in organic solvents. As a result, significantly higher gas concentrations can be achieved in the scCO$_2$ phase which may be advantageous in processing of nanostructured materials. For example, in reactive processes which involve such gases, higher concentrations in the fluid phase may result in higher reaction rates. The mass transfer limitations originating from the slow transfer of such gases across the gas–liquid interface may be eliminated.

In the synthesis of nanostructured materials using organic solvents, additional processing steps are generally required to remove the organic solvent from the material. An important advantage of scCO$_2$ is that it leaves no residue in the treated medium.

Companies manufacturing materials are faced with an ever-increasing solvent problem because of environmental concerns and therefore there is an ongoing trend in industry to replace toxic and hazardous solvents with less toxic or harmless solvents. Being a non-toxic solvent, scCO$_2$ has already replaced toxic organic solvents in a wide variety of applications and has tremendous potential for use in development of new environmentally friendly processes for synthesis of materials.

Supercritical fluid extraction (SFE) from a wide variety of matrices is practiced on a commercial scale with hundreds of plants in operation worldwide today. Some examples include extraction of hops and spices, decaffeination of coffee and tea, extraction of flavors, fragrances, and aromas from plants. In the last two decades, SCFs and especially scCO$_2$ has been attracting increasing attention as a solvent in processing of nanostructured materials due to its interesting properties. The first nanostructured material processed using a SCF and that has made its way to the mass market is an aerogel-based blanket for thermal insulation. The special property of a SCF that it does not go through a phase change during depressurization above its critical temperature has enabled the
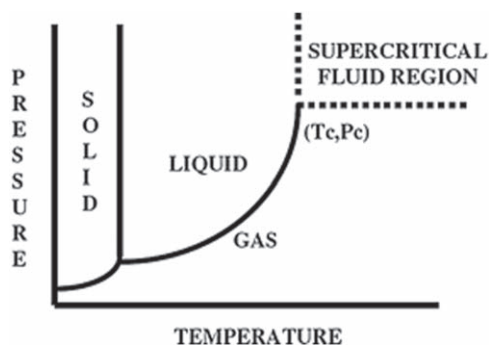
[z]E-mail: cerkey@ku.edu.tr

Figure 1. A typical *P–T* diagram of a pure compound.

Table I. Comparison of typical physical properties of gases, liquids, and SCFs.

Fluid properties	Gas	SCF	Liquid
Density (g cm^{-3})	$0.6–2 \times 10^{-3}$	0.2–0.9	0.6–1.6
Diffusivity (m^2 s^{-1})	$1–4 \times 10^{-5}$	$2–7 \times 10^{-8}$	10^{-9}
Viscosity (Pa s^{-1})	$1–3 \times 10^{-5}$	$1–9 \times 10^{-5}$	10^{-3}

development and production of these blankets with superior properties. The same property is also taken advantage in drying of microelectromechanical systems (MEMS) which is carried out using scCO$_2$ on a commercial scale. Recently, a process for impregnation of wood (a porous nanostructured material) with biocides using scCO$_2$ has been developed and commercialized in Denmark to treat 60,000 m^3 of wood every year. Again, the special properties of scCO$_2$ which are no residue on the treated medium and high rates of impregnation due to low viscosity and high diffusion coefficients have made this possible. It is highly likely that the number of nanostructured materials in the market which are produced using a SCF based technology will increase in the coming years. It has already been demonstrated in many laboratories around the world that SCFs can be a powerful medium to produce a wide variety of nanostructured functional materials such as films, nanoparticles, nanorods, nanowires, nanofibers, nano shish-kebaps with various morphologies including core-shell structures with superior properties.[1–3] Supercritical deposition is one of the SCF based technologies that has attracted significant interest in development of functional materials for electrochemical energy conversion and storage systems, primarily for fuel cells and electrolyzers. This review presents the fundamental aspects of SCD, properties of the materials obtained by SCD as well as their electrochemical performance and research needs.

Supercritical Deposition

Metals can be deposited on a variety of organic or inorganic supports using SCD in the form of supported dispersed species, nanoparticles, or films (Fig. 2). Using SCD, nanoparticles or films of metals and oxides including Cu, Co, Ni, Mo, Pt, Pd, Ru, Ag, Au, Rh, Ir, hafnium oxide, zirconia, yttria stabilized zirconia, ceria, titania, tantalum oxide, niobium oxide and bismuth oxides have been deposited on a wide variety of supports such as polymers, carbon materials and inorganic supports[1,4–16]

This technique was introduced by Watkins' group[17] and consists of the following steps:

1. The dissolution of a metal precursor in scCO$_2$,
2. The sorption, adsorption and/or surface reaction of the metal precursor from fluid phase to the support,
3. The conversion of the adsorbed metal precursor to its metal or metal oxide form,

The phase behavior of metal precursors in SCFs controls the first step in SCD technique i.e. the dissolution of metal precursor. Metal precursors usually used in SCD are metal chelates including β-ketonates, fluorinated β-ketonates and organometallic precursors. The solubility of the metal precursors with different ligand types including diketones, dithiocarbamates, macrocycles, organophosphorous ligands, hydroxamic acids in scCO$_2$ are available in the literature.[18–22] Precursors with fluorinated ligands have substantially higher solubilities as compared to their non-fluorinated analogues.[20] Carbonyl ligands also increase the solubility of a metal precursor due to its specific intermolecular interactions with CO$_2$.[23,24] The incorporation of more non-polar methyl or *tert*-butyl groups in the precursors also allows for the enhanced solubility.[18,25] Prediction of the solubility of metal precursors in scCO$_2$ is also possible using semi-empirical correlations or equation of state based methods.[21,26] Addition of small amounts of entrainers such as alcohols to scCO$_2$ can result in an increase in the solubility of metal precursors in scCO$_2$. Alcohols[27–30] and organic solvents[31–36] have been used to attain higher solubilities of metal precursors in scCO$_2$.

Türk's group studied the solid-liquid-gas behavior of some metal precursors in CO$_2$ by measuring the melting point depression curves for dimethyl (1, 5-cyclooctadiene) platinum (Pt(cod)me$_2$)[37,38] and bis (2, 2, 6, 6-tetramethyl-3, 5-heptadionato) copper (II) (Cu(thd)$_2$)[38] from 0.1 to 25.7 MPa. Melting point of Pt(cod)me$_2$ decreased from 105 °C at 0.1 MPa to 87 °C at 25.7 MPa whereas for Cu(thd)$_2$ the melting point decreased from 199 °C at 0.1 MPa to 126 °C at 19.7 MPa. There is a need to extend these studies to other precursors with different ligands for appropriate selection of operating conditions in SCD.

The second step in SCD is the adsorption of the precursor on the surface of the support. The adsorption isotherm reflects the amount of metal precursor that can be adsorbed on the support at a particular equilibrium concentration. It can also show the affinity of the metal precursor to the SCF and to the support. The interaction of the metal precursor with the support at different temperatures and pressures can also be quantified via the adsorption isotherm. The knowledge on the adsorption isotherm and adsorption kinetics of metal precursor-support system in SCF media is crucial for optimizing metal content. For high surface area supports such as carbon blacks, nanotubes, metal-organic frameworks or aerogels, the metal precursors are adsorbed on the interior surface of the porous solid particles. According to the published studies on adsorption thermodynamics of metal precursors onto porous supports in scCO$_2$, adsorption from scCO$_2$ usually results in monolayer surface coverage and can be represented by Langmuir type isotherms for metal precursors which have moderate solubility in CO$_2$.[39–43] For the case of metal precursors which have very low solubility in CO$_2$, the adsorption isotherms are linear.[39,44]

Adsorption kinetics measurements carried out either in static and dynamic fashion are available in the literature.[45] In the case of supports with high surface areas, it has been shown that the kinetics of adsorption of a metal precursor from scCO$_2$ can be modeled based on diffusion inside the pore volume by assuming local adsorption equilibrium between the metal precursor and support at the surface.[39,40,43,46]

The measurement and analysis of adsorption behavior in the presence of co-solvents requires caution.[47] Reported equilibrium concentration needs to be confirmed by assuring the presence of one single fluid phase. If there are multi-phases present, the position of support needs to be specified and the equilibrium concentration needs to be reported accordingly. The presence of CO$_2$ rich or organic-rich phases would cause partitioning of the solute and affect the data. Adsorption isotherms need to be measured at different co-solvent concentrations to clarify the effect of competitive adsorption. During the measurement and analysis of adsorption kinetics, all the precursor needs to be dissolved at the initial stage of the experiment. Adsorption isotherm parameters obtained at a particular co-solvent concentration should be used in the kinetics modeling of the corresponding co-solvent concentration only.
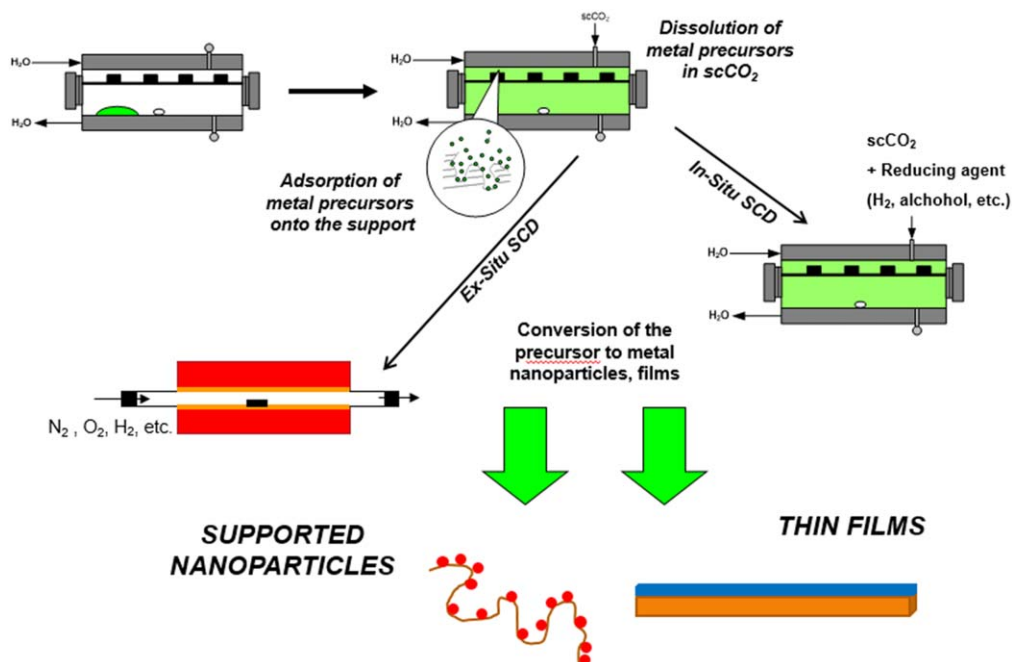
Figure 2. Schematic representation of the SCD process for the preparation of supported nanoparticles and films.

Thanks to extreme versatility of the SCD technique, a wide variety of methods can be used for the 3rd step where adsorbed precursors are converted to their metal forms[1,6] and one can end up with supported highly dispersed nanoparticles, films or rods. Figure 3 shows an exemplary Transmission electron microscopy (TEM) image and the associated particle size distribution for Pt nanoparticles supported on graphene aerogel (GA) prepared using SCD. These images show a mean particle size of 1.9 nm with a remarkably narrow particle size distribution considering a relatively high Pt loading of 32.9 wt.% for the sample.[48] The final properties of supported nanostructures such as size, distribution and morphology depend closely on the conversion method applied as well as the process parameters (reaction temperature and time) associated with the conversion step. The conversion step may be carried thermally, by a conversion agent such H_2, an alcohol or other reducing agents[49] either in $scCO_2$ (in situ conversion) or at low pressure after the depressurization (ex situ conversion) or by laser irradiation.[7,50] In SCD, the metal loading can be tuned via two different approaches; one can either adsorbed metal complexes onto the support in the presence of $scCO_2$ the value of which depends on the type of surface phenomena (adsorption/chemisorption/surface reaction) associated with the metal precursor-support system and then convert the adsorbed precursors to metal via ex situ route or one can use in situ conversion to convert all of the metal precursors initially placed in the vessel. Along this line, the effect of ligands of the metal precursor on the conversion to supported nanoparticles using SCD was studied by Aggarwal et al. and Wolff et al.[51,52]

There are two approaches to synthesize bimetallic or multi-metallic nanoparticles using SCD which are simultaneous[39,53] and sequential[54] deposition. In simultaneous SCD, one starts with two or more metal precursors by dissolving them simultaneously in $scCO_2$ and then carry out the same subsequent steps as in single component SCD whereas in sequential SCD, the single component SCD procedure is applied successively for each metal precursor. During simultaneous SCD, binary adsorption isotherms control the uptake of metal precursors in $scCO_2$ and these isotherms can elegantly be used
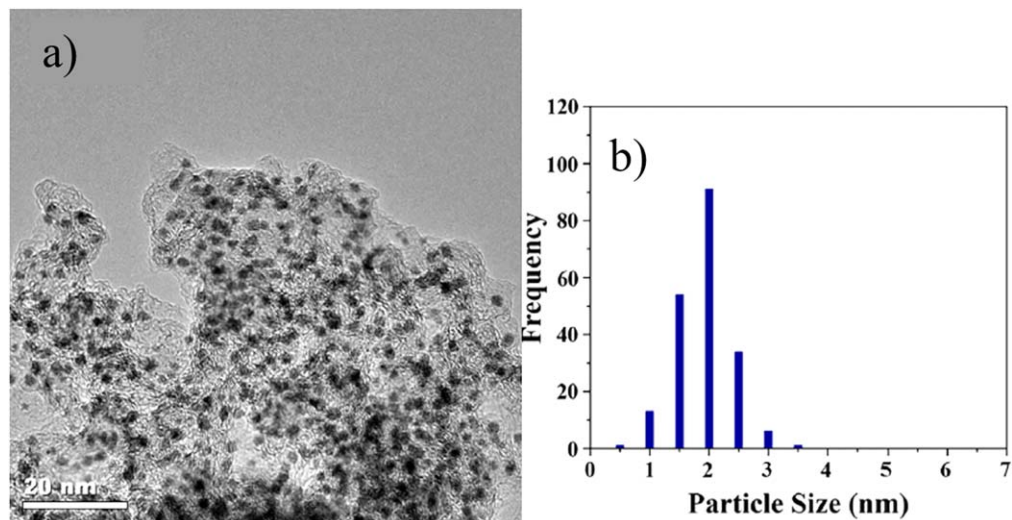

Figure 3. (a) Examplary TEM images of Pt/GA samples prepared using SCD (b) The particle size distribution of the image given in (a) Reprinted with permission from Ref. 48. Copyright © 2017, Elsevier.

to provide thermodynamic control over metal loading and concentration of metals within the supported bimetallic nanoparticles.[55]

Micro or nano-sized conformal films with high aspect ratio can be prepared via SCD in scCO$_2$ in the presence of reducing agents.[56,57] For the preparation of films using SCD, there are usually two different heating configurations within the reactors; hot wall[57,58] or cold wall.[56,57,59] Hot wall reactors are essentially isothermal furnaces and offer relatively easy temperature control. In cold wall reactors, the substrate is heated directly either by induction or by radiant heating while the rest of the reactor remains cooler. The reaction occurs on the heated substrate and the metal coating of the reactor walls is thus prevented.[60] These reactors can be operated in batch or continuous flow modes while taking advantage of the higher precursor concentrations in scCO$_2$.

Functional Materials for Electrochemical Applications Using Supercritical Deposition

Carbon supported nanoparticles.—The electrocatalytic activity of the supported mono/multi-metallic nanoparticles depends on several factors, such as support properties, metal content and dispersion, nanoparticle size and morphology which are strongly related to the preparation method. Supported metal nanoparticles can be prepared using various different techniques such as ion-exchange, wet impregnation, sol-gel, and chemical vapor deposition.[61–67] These conventional techniques are used widely; however, it is quite challenging to control the metal nanoparticle distribution, nanoparticle size, size distribution, metal loading, and nanocrystal orientation with these techniques.[1] SCD technique is an emerging approach for the preparation of supported nanoparticles that has several advantages over its counterparts[30,38,68–74] as explained in the previous section.

Carbon supported monometallic nanoparticles.—Fuel cell applications.—Fuel cells are promising devices for electricity production since their efficiencies are not bounded by Carnot cycle. However, they require specialized components such as electrocatalysts that have high precious metal loadings, separation membranes that are designed for permeation of specific ion(s) and gas diffusion layers that are designed for efficient transport of reactant gases and liquid products evolved. These specialized components contribute highly to the cost of the whole device. For example, according to the US Department of Energy's proton exchange membrane fuel cell (PEMFC) cost breakdown for 500,000 systems/year, membrane electrode assembly (MEA), which consists of membrane, electrocatalyst and gas diffusion layers, makes up more than 50% of the total cost, and become more significant at lower production rates (~64% for 1000 systems/year).[75] Furthermore, the ultimate target set for PEM fuel cell commercialization by DOE is 30 $ kW^{-1} for 500,000 systems/year. Research efforts, therefore, mainly focus on to reduce the cost while maximizing the efficiency. Better and cheaper electrocatalysts are definitely needed to meet these targets and SCD technology may enable the development of such materials.

The earliest study involving SCD to prepare electrocatalysts was conducted by Ye et al., who deposited Pd nanoparticles on multi-walled carbon nanotubes (MWCNTs) for oxygen reduction reaction (ORR). Palladium hexaflouroacetylacetonate hydrate (Pd(hfa)$_2$.xH$_2$O) precursor was adsorbed on MWCNTs at 80 °C and 8 MPa.[76,77] The conversion was carried out in situ in a mixture of CO$_2$ and H$_2$. TEM images showed that highly dispersed, spherical Pd nanoparticles with sizes in the range of 5–10 nm on the surface of the MWCNTs. Pd loading was determined gravimetrically as 10 wt%. X-ray photoemission spectroscopy (XPS) showed metallic Pd peaks, indicating Pd nanoparticles were formed on MWCNTs. Cyclic voltammograms taken in O$_2$ saturated electrolyte showed a cathodic current at 0.5 V (vs Ag/AgCl) attributed to O$_2$ reduction with onset potential shifted to more positive potentials when compared to literature showing the high electrocatalytic activity of Pd/MWCNT.[78] Stability of the electrocatalyst was investigated at 0 V (vs Ag/AgCl) for 14 h by

continuously bubbling O$_2$ and no loss was observed in current density indicating the high stability. ORR reaction mechanism on Pd/MWCNT followed a 2-electron pathway since the addition of H$_2$O$_2$ increased the reduction current. Although, conversion is beneficial for high utilization of metal precursors, fluorinated functional groups are quite hard to remove from the surface at moderate temperatures and H$_2$ is usually required to clean the surface which also results in higher nanoparticle size and broader size distribution. The authors also prepared Pt/MWCNT electrocatalyst by SCD for direct methanol fuel cells (DMFCs).[68] Methanol was also added as co-solvent to adjust the polarity of the mixture in order to completely dissolve platinum (II) acetyl acetonate (Pt(acac)$_2$) precursor in scCO$_2$ at 200 °C and 8 MPa. Pt(acac)$_2$ was converted by introducing CO$_2$ and H$_2$ at 12 MPa. TEM images showed uniformly dispersed Pt nanoparticles on the MWCNT with sizes in the range of 5–10 nm. Energy-dispersive X-ray spectroscopy (EDXS) analysis showed 25 wt.% Pt loading on MWCNT. XPS also confirmed that most of the Pt on MWCNT surface was in the metallic form. Cyclic voltammograms obtained in N$_2$ saturated 0.5 M H$_2$SO$_4$ electrolyte showed only one peak at 0.45 V (vs Ag/AgCl) in the cathodic direction attributed to the reduction of Pt-oxides, indicating that Pt nanoparticles had a clean surface. Cyclic voltammograms in O$_2$ saturated electrolyte showed a broad peak arising from Pt-oxide reduction and O$_2$ reduction. The calculated Tafel slope for Pt/MWCNT was −21 mV decade^{-1} which was lower than the Tafel slope for the same electrocatalyst prepared by electrodeposition.[79] Moreover, Pt/MWCNT gave an exchange current density one order-of-magnitude higher than the commercial Pt/C at a lower Pt loading indicating that SCD resulted in highly active electrocatalysts. Methanol oxidation performance of Pt/MWCNT was also investigated by cyclic voltammetry (CV). The ratio of the forward peak current (I$_f$) to the reverse peak current (I$_b$) was reported as 1.4. A high I$_f$/I$_b$ ratio signifies the high capability of prepared Pt/MWCNT electrocatalyst to oxidize intermediate carbonaceous species which is considered as catalyst poison.

Zhao et al. also followed a similar procedure to prepare Pt and Pd nanoparticles on various supports for DMFCs.[80,81] Pt(acac)$_2$ and Pd(hfa)$_2$ were used as metal precursors and methanol was added to adjust the polarizability of scCO$_2$ in order to completely dissolve the metal precursors. Graphene sheet (GS) and Vulcan (CB) supported Pt electrocatalyst were prepared at 200 °C and 12 MPa for 1.5 h followed by in situ conversion with the injection of CO$_2$ and H$_2$ mixture at 16 MPa. The reactor was heated to 300 °C and kept at these conditions for 1.5 h.[80] Pristine graphene (PG), reduced graphene oxide (RGO), MWCNT and, CB supported Pd were prepared at 50 °C and 18 MPa with the addition of dimethyl amine borane (C$_2$H$_7$BN) as reducing agent and kept at these conditions for 5 h.[81] RGO supported Pd(hfa)$_2$, however, was converted at 180 °C to completely reduce the GO. TEM images of the prepared Pt/GS and Pt/CB electrocatalysts showed dispersed Pt nanoparticles with little agglomeration probably due to utilization of methanol as co-solvent since same phenomena was also observed for Pd electrocatalyst prepared in a similar manner. The average Pt nanoparticle sizes were determined as 3.3 and 5.2 nm for Pt/GS and Pt/CB, respectively. Similar average nanoparticle sizes were obtained for Pd/PG and Pd/CB as 3.6 and 5.0 nm, respectively, indicating that support-solvent interaction plays an important role in the resulting average nanoparticle size. On the other hand, Pd/RGO and Pd/MWCNT had significantly higher average Pd nanoparticle sizes (8.1 and 7.4 nm, respectively). Electrochemically active surface area (ESA) of Pt/GS (41.5 m^2 g^{-1}) was significantly higher than the ESA of Pt/CB (19.2 m^2 g^{-1}) due to smaller nanoparticle size of Pt/GS providing more accessible electrochemical active sites. On the other hand, Pd/PG electrocatalyst had a remarkable ESA of 115.0 m^2 g^{-1} which was substantially higher than the ESA of Pd/RGO (53.9 m^2 g^{-1}), Pd/CNT (30.8 m^2 g^{-1}) and Pd/CB (12.9 m^2 g^{-1}). Since these values were higher than or comparable to the ESA of Pt electrocatalyst on similar supports, it was suggested that Pd can be a viable replacement for Pt in DMFC applications. Furthermore, prepared Pd electrocatalysts also had high ESA values in alkaline media. Mass

activities of Pd-based electrocatalysts were also higher than the mass activities of Pt-based electrocatalysts; however, in both cases the reported mass activities were higher than the literature values indicating that SCD is an effective tool for the preparation of highly active electrocatalysts.

Later, Zhao et al. investigated the electrocatalytic activity of GS, MWCNT and Vulcan (C) supported Pt nanoparticles via SCD for DMFCs without the addition of co-solvent.[82] Supported nanocomposites were prepared at 70 °C and 24.5 MPa for 6 h using Pt(cod)me$_2$ as Pt precursor followed by ex situ conversion at 200 °C for 4 h under flowing N$_2$. Pt loadings of electrocatalysts were determined both gravimetrically and with inductively coupled plasma optical emission spectroscopy (ICP-OES) as 31 wt.%, 31 wt. % and, 11 wt.% for Pt/GS, Pt/MWCNT and Pt/C. The lower Pt loading at Pt/C was attributed to weaker affinity of Vulcan to Pt(cod)me$_2$; however, lower surface area of Vulcan could also play an important role in the low uptake amount. TEM images of Pt/GS showed extremely dispersed Pt nanoparticles on GS with average Pt nanoparticle size of 2.2 nm which is smaller than the average Pt nanoparticle sizes obtained via wet impregnation method (3– 5 nm).[83,84] This value is also smaller than authors' previous study were methanol was used as co-solvent to dissolve Pt(acac)$_2$.[80] This may be due to co-solvent addition that may alter the partitioning of the precursor in scCO$_2$ resulting in different adsorption thermodynamics. TEM images of Pt/MWCNT also showed dispersed Pt nanoparticles with a slightly higher average nanoparticle sizes (2.9 nm), whereas Pt/C had significantly larger average nanoparticle size (5.93 nm) at significantly lower Pt content (11 wt.%) similar to previous study.[80] Increasing the Pt loading of Pt/GS electrocatalysts to 60 wt.% and 80 wt.% did not affect the homogenous distribution or the average nanoparticle size. Moreover, commercial Pt/C electrocatalyst with 20 wt.% Pt loading and average Pt nanoparticle size of 3 nm was characterized for comparison since Pt/C prepared via SCD had very low Pt loading. ESA values were determined as 44.3 m^2 g^{-1}, 32.8 m^2 g^{-1} and, 30.1 m^2 g^{-1} for Pt/GS, Pt/MWCNT and, commercial Pt/C, respectively. Higher ESA of Pt/GS was attributed to smaller average Pt nanoparticle size. Both Pt/GS and Pt/MWCNT had lower onset potential (0.13 and 0.18 V (vs Ag/AgCl), respectively) for methanol electrooxidation than commercial Pt/C (0.20 V (vs Ag/AgCl)) indicating the high activity of the electrocatalysts prepared via SCD. Furthermore, Pt/GS electrocatalyst had superior mass activity and I$_f$/I$_b$ ratio than Pt/MWCNT and commercial Pt/C. Said-Galiyev et al. also investigated electrochemical performance of the Pt nanoparticles supported on different carbons (Acetylene Black (AC-1) and Vulcan XC72R) prepared via SCD towards methanol electrooxidation.[85] Adsorption of Pt(cod)me$_2$ precursor on supports were conducted at 120 °C and 25 MPa for 6 h. Conversion of the precursor was carried out using CO$_2$ or Ar flow at 150 °C–230 °C and at 0.3–30 MPa for 3–6 h. TEM images showed that the size of Pt nanoparticles ranged between 2 and 2.4 nm (very narrow particle size distribution) even at Pt loadings as high as 40 wt.%, whereas, commercial Pt/C catalysts showed non-uniform distribution of Pt nanoparticles with significant agglomeration. Cyclic voltammograms of the prepared electrocatalysts were featureless in the hydrogen adsorption/desorption region due to poisoning from the cyclooctadiene ligand suggesting that during conversion, ligands of the precursor were not removed from the surface. Therefore, before cyclic voltammetry, surface of the electrocatalysts was cleaned by means of CO adsorption/desorption. Methanol electrooxidation runs revealed electrocatalysts prepared via SCD were less prone to self-poisoning at the potential interval of interest. Specific activities were determined from the steady-state polarization curves and Pt/C electrocatalysts prepared with SCD had higher specific activities when compared to commercial Pt/C electrocatalysts.

Taylor et al. investigated the factors which affected Pt nanoparticle size on various carbonaceous supports (carbon black (XC-72), carbon fiber (CF) and single-walled carbon nanotubes (SWCNTs)) in SCD in high-temperature liquid methanol and in supercritical

methanol using Pt(acac)$_2$ as Pt precursor.[86] Furthermore, authors also studied the addition of sodium dodecyl sulfate (SDS) to functionalize support materials to anchor more Pt nanoparticles on the surface. High-resolution transmission electron microscopy (HRTEM) images showed dispersed Pt nanoparticles on support with a relatively narrow particle size distribution. In supercritical methanol, the average Pt nanoparticle sizes was lower than 5 nm; on the other hand, when scCO$_2$ was used as the SCF, average Pt nanoparticle size was greater than 5 nm. This was attributed to absence of H$_2$ since at those temperatures supercritical methanol acted as a reducing agent. In supercritical methanol, at the same density, temperature had little effect on the Pt particle size, whereas, decreasing density resulted in higher average Pt nanoparticle size with broader size distribution. However, all reported particle sizes were quite close to each other. Furthermore, deposition medium affected nanoparticle nucleation and growth. Furthermore, increasing the deposition time only slightly increased the average Pt nanoparticle size. Electrocatalytic tests were performed in a single-cell fuel cell set-up with anode and cathode loadings of 0.5 mg cm^{-2}. Cathode electrocatalyst was commercial Pt/C with 20 wt.% Pt loading whereas anode electrocatalyst was Pt/CF, Pt/XC-72 and Pt/ SWCNT prepared by SCD. From the polarization curves and peak power density values, SDS addition increased the electrochemical activity attributed to the Pt nanoparticle yield increase with SDS addition. Pt/SWCNT modified with SDS gave the best electrochemical performance with peak power density of 449 mW cm^{-2} which was higher than peak power density of commercial Pt/C and a Pt utilization of 919 mW mg$_{Pt}^{-1}$. Although supercritical methanol can be advantageous to dissolve cheaper and more available metal precursors, it has a much higher Tc (240 °C) than CO$_2$ (31.2 °C) which results in high energy consumption. Methanol is flammable at such high temperatures and pressures which requires caution. Furthermore, methanol is liquid at ambient conditions which requires additional solvent removal steps.

Shimizu et al. also utilized MWCNT as electrocatalyst support for Pt nanoparticles, but they investigated three different mediums from which adsorption took place.[87] These were (i) scCO$_2$ with Pt(acac)$_2$ at 200 °C and 12 MPa for 1 h (Pt/MWCNT-SC), (ii) water-in-hexane microemulsion with sodium tetrachloroplatinate(II) (Na$_2$PtCl$_4$) and surfactant 2-ethyl hexyl sulfosuccinate (AOT) at room temperature for 30 min (Pt/MWCNT-ME), and (iii) water-in-scCO$_2$ microemulsion with Na$_2$PtCl$_4$ solution, AOT and hexane at 40 °C and 19 Mpa for 1.5 h (Pt/MWCNT-SCME). At each route, the adsorbed Pt precursor was converted using H$_2$ as reducing agent. TEM images showed that Pt/MWCNT-SCME electrocatalysts had highly dispersed Pt nanoparticles on MWCNTs similar to Pt/ MWCNT-ME indicating that water-in-scCO$_2$ microemulsion was a viable medium for SCD to prepare supported nanoparticles. X-ray diffraction (XRD) of Pt/MWCNT-SCME had fcc peaks of metallic Pt and average Pt nanoparticle sizes were calculated using Scherer equation as 8.7 nm whereas Pt/MWCNT-SC had Pt nanoparticle sizes in the range of 5–10 nm; however, average Pt nanoparticle size for Pt/MWCNT-ME was not given. Highest ESA was obtained with Pt/MWCNT-SCME as 31.1 m^2 g$_{Pt}^{-1}$, On the other hand, Pt/ MWCNT-SC had the lowest ESA as 6.04 m^2 g^{-1}. Authors attributed the high ESA of Pt/MWCNT-SCME to efficient removal of surfactant when scCO$_2$ was used as co-solvent instead of hexane. However, they did not explain the very low ESA of Pt/MWCNT-SC. At 1 A g$_{Pt}^{-1}$, Pt/MWCNT-SCME exhibited a positive shift in the ORR curve by 100 mV as compared to commercial Pt/C and this difference became more pronounced at higher A g$_{Pt}^{-1}$ values showing that Pt/MWCNT-SCME had high activity towards ORR. The mass activities were obtained from the chronoamperometric measurements at 30 s. Pt/MWCNT-SCME gave 5-fold higher mass activity when compared to commercial Pt/C attributed to the high ESA. Furthermore, electron transfer numbers were 3.7, 3.4, 3.1 and, 2.9 for Pt/MWCNT-SCME, Pt/MWCNT-SC, commercial Pt/C and, Pt/MWCNT-ME, respectively indicating that complete conversion of O$_2$ to H$_2$O was most efficient with Pt/MWCNT-SCME

electrocatalyst. Since it is desired to decorate the outer surface of MWCNTs with metallic nanoparticles water-in-CO_2 microemulsions can be a viable medium. However, caution must be taken with microemulsions when dealing with highly porous supports, because the size of the water pools surrounded by surfactant molecules can be substantially larger than the pore size of the support which prevents penetration to the pores and thus decrease loading.

Erkey's group extensively investigated the preparation of electrocatalysts via SCD.[48,88–91] Bayrakçeken et al. investigated ORR activity of Pt nanoparticles on different support materials (MWCNT, Vulcan, BP2000) prepared via SCD.[88] Pt(cod)me$_2$ was used as Pt precursor and adsorption on the supports was carried out at 70 °C and 24.2 MPa for 6 h. Afterwards, conversion of adsorbed Pt precursor was carried out ex situ at 200 °C under flowing N_2 for 4 h. XRD of the prepared electrocatalysts showed the fcc peaks of metallic Pt demonstrating that Pt nanoparticles were successfully formed on carbonaceous supports. Average Pt nanoparticle sizes determined from the XRD were in the range of 1–2 nm for the electrocatalysts prepared via SCD whereas commercial Pt/C (ETEK) had an average Pt nanoparticle size of 6 nm showing that SCD is a powerful technique to prepare supported nanoparticles. HRTEM images showed highly dispersed Pt nanoparticle on all supports with sizes in the range 1–2 nm in agreement with XRD whereas commercial electrocatalyst (ETEK) had some agglomerated Pt nanoparticles. Highest Pt loading was obtained with BP2000 as 47.5 wt.% due to the high surface area whereas 9–10 wt.% Pt loading was achieved for MWCNT and Vulcan. Although, Pt/BP2000 had the highest Pt loading, Pt/Vulcan had the highest ESA attributed to the higher pore volume of BP2000 in which some of the Pt nanoparticles could become inaccessible to the electrolyte. Among prepared electrocatalysts, Pt/MWCNT had the highest Pt utilization value of 93% whereas commercial Pt/C (ETEK) had a Pt utilization over 100% which could be due the broad particle size distribution. Electron transfer numbers were 3.5, 3.6 and 3.7 for Pt/BP2000, Pt/Vulcan and Pt/MWCNT, respectively, signifying that prepared electrocatalyst had low H_2O_2 production. However, mass and specific activity of the electrocatalysts were not provided. Preparation of Vulcan supported Pt electrocatalysts with SCD was further investigated by Bayrakçeken et al. using Pt(cod)me$_2$ as Pt precursor.[89] The effect of conversion route to the electrochemical activity was investigated using two different conversion routes: (i) ex situ thermal reduction under flowing N_2, and (ii) in situ thermal conversion in scCO$_2$. For the first route, adsorption was carried out at 70 °C and 24.2 MPa for 6 h followed by ex situ conversion at 200 °C under flowing N_2 for 4 h. For the second route, adsorption was carried out at 70 °C and 13.6 MPa for 12 h. Afterwards, temperature was raised to 140 °C for in situ conversion which increased the pressure to 31.0 MPa and maintained at these conditions for 6 h. The Pt loadings were determined as 9 wt.% for route (i) and 15 wt.% and 35 wt.% for route (ii). in situ conversion route can be beneficial for efficient utilization of the high priced

organometallic precursors since all of the precursor can be adsorbed and converted on the support, whereas, ex situ conversion route follows the adsorption equilibria of the precursor-support-solvent system which means that a certain amount of the metal precursor stays in the fluid phase and removed with the solvent at depressurization TEM images showed highly dispersed Pt nanoparticles on Vulcan surface with extremely narrow particle size distributions. XRD also showed the fcc peaks of the metallic Pt indicating that successful conversion of Pt(cod)me$_2$ was achieved in both routes. Average Pt nanoparticle sizes were calculated from XRD as 1.2, 1.3 and 2 nm for Pt loadings of 9 wt.%, 15 wt.% and 35 wt.%, respectively in agreement with TEM. ESA values were determined as 173, 125 and 87 m^2 g$_{Pt}^{-1}$ for Pt loadings of 9 wt.%, 15 wt.% and 35 wt.%, respectively. However, no comparison was given to literature or commercial Pt/C. Bozbag et al. also investigated the effect of different conversion routes on the ORR activity of Vulcan supported Pt electrocatalysts prepared via SCD.[90] Adsorption of Pt(cod)me$_2$ was carried out at 50 °C and 13.2 MPa for 12 h. Three different conversion routes were investigated as follows: (i) ex situ thermal conversion at 200 °C under flowing N_2 for 4 h, (ii) in situ thermal reduction in scCO$_2$ by heating the reactor to 120 °C which increased the pressure to 26.9 MPa and kept at these conditions for 6 h, and (iii) ex situ chemical conversion at 200 °C under flowing H_2 for 4 h. Pt nanoparticles were formed as evident from the fcc peaks of metallic Pt in XRD. Average Pt nanoparticle sizes obtained from TEM images were 1.6, 2.5 and 3 nm for routes (i), (ii) and, (iii), respectively indicating that conversion route had a significant effect on the particle size distribution. Although, route (i) resulted in smaller average Pt nanoparticle size, the highest ESA was obtained for route (ii) as 92.2 m^2 g^{-1}. This was attributed to the microporosity of Vulcan in which very small nanoparticles could be trapped and became inaccessible to electrolyte. Similar trend in activities was observed as ESAs; route (ii) gave the highest mass activity as 0.11 A mg$_{Pt}^{-1}$ which was the same as commercial Pt/C.[92] On the other hand, specific activity of route (i) and (ii) were basically the same. The lowest mass and specific activity values were obtained for route (iii) as expected due to large Pt nanoparticle size since ORR activity strongly correlated with the average Pt nanoparticle size.[93] Furthermore, electrocatalysts were tested in a single-cell PEMFC setup with highest power density and Pt utilization were obtained for route (i) as 190 mW cm^{-2} and 380 mW mg$_{Pt}^{-1}$, respectively. More recently, Barim et al. investigated the controlled growth of Pt nanoparticles on carbon aerogels (CA) with different pore sizes (4, 6 and 19 nm) by SCD as electrocatalysts for PEMFCs.[91] CAs have very high surface areas (400–1500 m^2 g^{-1}), low mass densities, sharp pore size distributions and very high electrical conductivities that makes them promising as electrocatalyst supports since the ideal support should have high accessible surface area, suitable pore size and pore volume for efficient ion transport and high electrical conductivity, CAs could therefore be promising candidates as electrocatalyst support.[94–99] Adsorption Pt(cod)me$_2$ was carried out
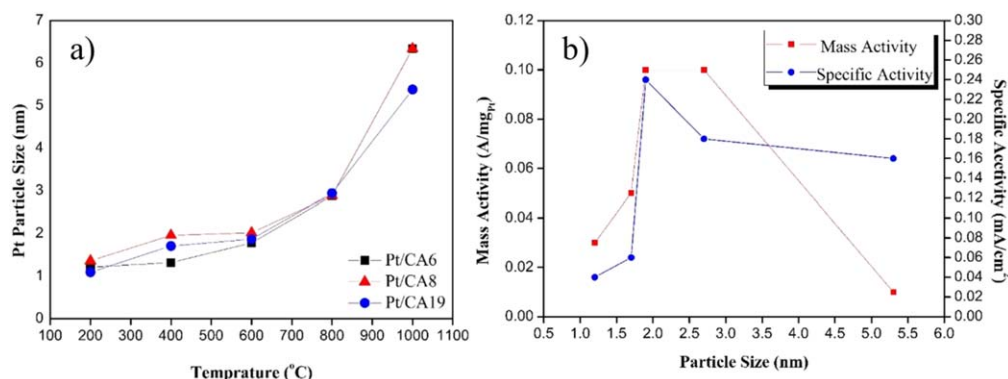

Figure 4. (a) Average Pt nanoparticles sizes of Pt/CAs with corresponding conversion temperatures. (b) Mass and specific activity trends of Pt/CA19 electrocatalysts with increasing Pt nanoparticle sizes. Reprinted with permission from Ref. 91. Copyright © 2017, Elsevier.

at 80 °C and 27.6 MPa for 24 h. Afterwards, Pt precursor was converted via ex situ heat treatment under N_2 flow at different temperatures (200 °C–1000 °C). Conversion temperature primarily governed the resulting average nanoparticle size regardless of the pore size of the CA. Increasing conversion temperatures increased the average nanoparticle size without significant agglomeration. Pt nanoparticles in the range of 1.1 nm (200 °C) and 5.6 nm (1000 °C) were obtained showing that precise particle size control is possible with SCD (Fig. 4a). ESA values were calculated for 10th and 200th cycles and Pt/CA19 samples showed the highest ESA values. Furthermore, Pt/CA4 and Pt/CA8 did not exhibit significant mass or specific activity values towards ORR attributed to the lower pore size of these supports that resulted in pore blockage with the addition of Nafion® hence decreasing the number of accessible active sites. Pt/CA19 electrocatalysts, on the other hand, showed a similar trend of mass and specific activity values with increasing Pt nanoparticle size (Fig. 4b) to that reported previously in the literature.[93]

Along similar lines, Oztuna et al. prepared GA supported Pt electrocatalysts for ORR via SCD.[48] They also investigated the effect of precursor conversion temperature on average Pt nanoparticle size and electrocatalytic activity towards ORR. Adsorption was conducted at 35 °C and 10.7 MPa for 24 h using $Pt(cod)me_2$ as Pt precursor followed by ex situ conversion under flowing N_2 at various temperatures (200 °C–800 °C). XRD showed that at 200 °C precursor conversion was not complete unlike in the case of Pt/CAs[91] probably due to different surface chemistries of GA and CA. On the other hand, average Pt nanoparticle sizes obtained from TEM images were almost identical in Pt/GAs as in Pt/CAs at the corresponding conversion temperatures and similar Pt loadings indicating that precise control of nanoparticle size is possible with SCD. Highly dispersed Pt nanoparticles were obtained on GA surface as evident from TEM images with the average Pt nanoparticle sizes in the range 1.7 nm (400 °C) and 2.9 nm (800 °C). Moreover, XPS C 1 s spectra of the electrocatalysts and blank GA showed that during thermal treatment, Pt precursor conversion and nanoparticle growth occurred simultaneously with the reduction of the functional groups on GAs which caused more defect sites that Pt nanoparticles can anchor. Enhanced ESA was obtained with Pt/GA (600 °C) as 102 m^2 g^{-1} and decreased with increasing Pt nanoparticle size of Pt/GA(800 °C), as expected. Although Pt/GA (400 °C) had the smallest average Pt nanoparticle size, its ESA was lower than Pt/GA(600 °C) attributed to the uncompleted reduction of functional groups on GA which could bind to Pt active sites decreasing the ESA. Pt/GA(400 °C) and Pt/GA(600 °C) exhibited 3–4 fold higher mass activities towards ORR than the ones reported in the literature for Pt/GAs prepared via solvothermal routes.[100,101] Moreover, Pt/GA(800 °C) exhibited 3-fold higher activity than the ones reported in the literature.[101] However, stability tests showed that Pt/GA electrocatalysts rapidly degraded with continuous potential cycling indicating there is still room for improvement. Precise control of Pt nanoparticle size is extremely important to obtain highly active electrocatalysts since ORR is a particle size dependent reaction. Mass and specific activity increases up to a certain Pt nanoparticle size (~2.5 nm) above which mass activity decreases significantly and specific activity remains the same .[93] As evident from the Pt single crystal studies, Pt {111} facet is the ORR active site and below a certain Pt nanoparticle size Pt {100} and Pt {110} facets are predominant over Pt {111} resulting in low ORR activity.[102]

Ang et al. compared the ORR activity of Pt/Vulcan electrocatalysts prepared via wet impregnation and SCD.[103] For wet impregnation route hexachloroplatinic acid (H_2PtCl_6) was used as Pt precursor and pH was adjusted to 10 with the dropwise addition of sodium hydroxide (NaOH) at room temperature. Reduction of the Pt precursor was carried out at room temperature for 12 h using sodium borohydrate ($NaBH_4$) as reducing agent. For SCD, $Pt(cod)me_2$ was used as Pt precursor and adsorption was carried out at 40 °C and 8.3 MPa for 12 h. Conversion was carried out ex situ under flowing N_2 at 300 °C for 3 h. Pt loadings were determined via TGA as 30 wt.%

and 24 wt.% for Pt/C(H_2O) and Pt/C($scCO_2$), respectively. TEM images showed dispersed nanoparticles on Vulcan with Pt/C($scCO_2$) had a narrower particle size distribution. The average Pt nanoparticle sizes were determined as 4.2 nm and 3.7 nm for Pt/C(H_2O) and Pt/C($scCO_2$), respectively. Wet impregnation method yielded higher average Pt nanoparticle size although reduction of the precursor was conducted at room temperature showing that SCD could be utilized to obtain small nanoparticles dispersed on support material. ESA values were determined as 1.15 cm^2 and 1.0 cm^2 for Pt/C($scCO_2$) and Pt/C(H_2O), respectively. Authors attributed the higher ESA of Pt/C($scCO_2$) to lower nanoparticle size; however, the values are not normalized to Pt amount on the electrode. Electron transfer numbers were 4.0 and 4.1 for Pt/C($scCO_2$) and Pt/C(H_2O), respectively, demonstrating that both electrocatalysts converted O_2 to H_2O without any production of H_2O_2. Stability of the electrocatalysts were determined through continuous potential cycling (5000 cycles). After potential cycling Pt/C(H_2O) lost 23% of its ESA, whereas Pt/C($scCO_2$) had no loss. TEM images after accelerated stress tests showed significant growth in Pt nanoparticles in the case of Pt/C(H_2O) with an average Pt nanoparticle size of 9.2 nm whereas only slight growth was observed for Pt/C($scCO_2$) (5.5 nm) attributed to the solvation properties of $scCO_2$ indicating that SCD resulted in highly stable electrocatalysts.

Due to high cost of Pt-group metals (PGMs) (i.e., Pt, Pd, Ir, Os, Rh and Ru) commercialization of fuel cells are hindered, therefore, research efforts are recently directed to develop electrocatalysts containing non-PGM elements, such as Fe and Co.[104–108] Lai et al. investigated the ORR activity of lignin derived electrospun carbon nanofiber mat (ECNF) supported Ag nanoparticles via SCD in alkaline media.[109] Adsorption was conducted at 36 °C and 17.2 MPa for 24 h using (1,5cyclooctadiane) (hexaflouroacetylacetonato) silver (I) (Ag(hfa)COD) in $scCO_2$. Conversion of the Ag precursor were carried out ex situ at 180 °C for 3 h under flowing N_2/H_2 mixture. Ag loading was determined gravimetrically as 11, 15 and 25 wt.%. TEM images of Ag(hfa)COD-ECNF showed some dark spots indicating that some of the Ag precursor were converted during deposition step; however, upon thermal treatment Ag nanoparticles grew significantly and could be seen in scanning electron microscopy images (SEM) as uniformly distributed particles on ECNFs' surface. XRD of Ag(hfa)COD-ECNF also showed fcc peaks of metallic Ag confirming that Ag precursor is reduced during SCD. After thermal treatment, Ag nanoparticle size increased. Increasing Ag loading also increased the Ag nanoparticle size but did not change the morphology significantly. Ag/ECNF electrocatalyst with 15 wt.% loading had the highest oxidation/reduction current density as evident from the Ag oxidation peak at 0.15–0.4 V (vs Ag/AgCl) and Ag reduction peak at around 0 V (vs. Ag/AgCl). Rotating ring-disk electrode experiments (RRDE) were conducted at same conditions with rotation speeds between 100–2500 rpm. Ag/ECNF electrocatalyst with 11 wt.% Ag loading yielded only 10% H_2O_2 with an electron transfer number of 3.9, same as commercial Pt/C; however, H_2O_2 yield increased with increasing Ag nanoparticle size. Furthermore, mass activities were 119 mA mg^{-1} and 98 mA mg^{-1} for Ag/ECNF (15 wt%) and commercial Pt/C, respectively, showing that Ag can be a viable replacement for Pt in AFCs. However, the activity in the acidic media was not reported.

More recently, Unsal et al. developed novel N-doped CA supported Co electrocatalysts via SCD coupled with NH_3 for ORR in alkaline media.[110] For this purpose, cobalt (III) acetylacetonate ($Co(acac)_3$)-resorcinol formaldehyde aerogel (RFA) composites were prepared via SCD at 70 °C and 20 MPa followed by the carbonization and simultaneous N-doping under flowing NH_3 at elevated temperatures (700 °C–1000 °C) for 6 h. N-doped Co/CA samples had Co nanoparticles with C-shells at pyrolysis temperatures 800 °C and higher. Optimum carbonization temperature was determined as 800 °C based on the ORR activity. N-doping was necessary to obtain high ORR activity as evident from the onset potentials. Rotating disk electrode (RDE) experiments in alkaline media showed that ORR followed a 4 e^- pathway on N-doped Co/

CA (800 °C) with an onset potential of 0.92 V (vs RHE) which was close to commercial Pt/C (0.95 V (vs RHE)) signifying that SCD coupled with NH_3 is a promising route to obtain active non-PGM electrocatalysts. Moreover, authors performed post acid-base treatments to reveal the nature of the active sites and reported that high ORR activity was a result of the synergistic effects of Co nanoparticles and N-doping.

Electrolyzer applications.—PEM electrolyzers are devices which convert water to hydrogen and oxygen on electrocatalyst surfaces. The energy obtained from renewable energy resources such as sun, wind and hydrothermal, can be utilized for the electrolysis of water storing it in the chemical bonds of hydrogen. Electrolyzers produce extremely pure hydrogen without any harmful emission making them suitable for use with hydrogen fuel cells to obtain a sustainable energy. Electrocatalyst preparation via SCD for water splitting reactions was also investigated in the recent years in light of the promising electrocatalytic activities obtained for fuel cells with SCD.[111,112] Chen et al. prepared graphene-like layered carbon (GLC) supported Ru nanoparticles via SCD with scH$_2$O.[111] SCD experiments were conducted at 400 °C for 10 min with ruthenium chloride (RuCl$_3$) as Ru precursor via simultaneous adsorption and conversion of the precursor on GLC with Ru loadings in the range 2–62 wt.%. As can be seen from the TEM images, even at high loadings dispersed Ru nanoparticles without agglomeration was obtained with average nanoparticle sizes in the range of 2–5 nm (Fig. 5). The prepared Ru/GLC (10 wt.%) electrocatalyst had significantly smaller onset potential for hydrogen evolution reaction (HER) (3 mV) when compared to commercial Ru/C (22 mV) at the same metal loading demonstrating high activity. At current density value of 10 mA cm^{-2}, an overpotential of 35 mV was obtained for Ru/GLC which was nearly 2-fold lower than commercial Ru/C and also lower than the previously reported HER electrocatalysts in the literature.[113–116] Furthermore, Ru/GLC electrocatalyst had a Tafel slope of 46 mV decade^{-1} lower than the commercial Ru/C

signifying the high electrocatalytic activity. Similarly, Thangasamy et al. prepared Mo$_2$S/MWCNT electrocatalysts using DMF as SCF at 400 °C for 30 min using ammonium tetrathiomolybdate (ATTM) as Mo$_2$S precursor.[112] TEM images indicated that MWCNT surface became rougher after SCD and Mo$_2$S nanoparticles in the range of 20–50 nm were uniformly dispersed on the surface (Fig. 6a). EDS was used to confirm the Mo:S mole ratio to be 2:1 so that the nanoparticles had Mo$_2$S composition. Electrocatalytic activity of the Mo$_2$S/MWCNTs were determined through linear sweep voltammetry analysis (LSV). In light of the LSV results, Mo$_2$S/MWCNT had lower onset potential for HER than previously reported electrocatalysts (Fig. 6b). Furthermore, Tafel slope value for Mo$_2$S/MWCNT suggested that HER follows Volmer-Heyrovsky mechanism. Stability tests showed that Mo$_2$S/MWCNT had negligible loss in the cathodic current density after 1000 cycles indicating high stability. These studies also indicate that cheaper metallic salts can be utilized as metal precursors with polar SCF such as H$_2$O and DMF, however, there are several drawbacks. For example, carbon support can easily be corroded due to highly oxidative properties of H$_2$O at high temperature and pressure requiring very short deposition durations that may be insufficient to obtain desired metal loadings. Moreover, when SCFs that are liquids at ambient temperature and pressure were used as medium, additional solvent removal step is required which may have a profound effect on the morphology of the material. Alternatively, metallic salts can be dissolved in environmentally benign CO$_2$ to some extent with the addition of a co-solvent (usually an alcohol).

Increasing CO$_2$ levels in the atmosphere due to continuous consumption of fossil fuels has been identified as the main reason of global warming.[117,118] It is imperative to convert CO$_2$ to more value-added hydrocarbon products or intermediates via sustainable routes since conventional CO$_2$ reduction is carried out at high temperatures which requires energy that is generally obtained from fossil fuels.[119–122] Among several energy conversion routes electrical-to-chemical energy conversion stands out for its high-power
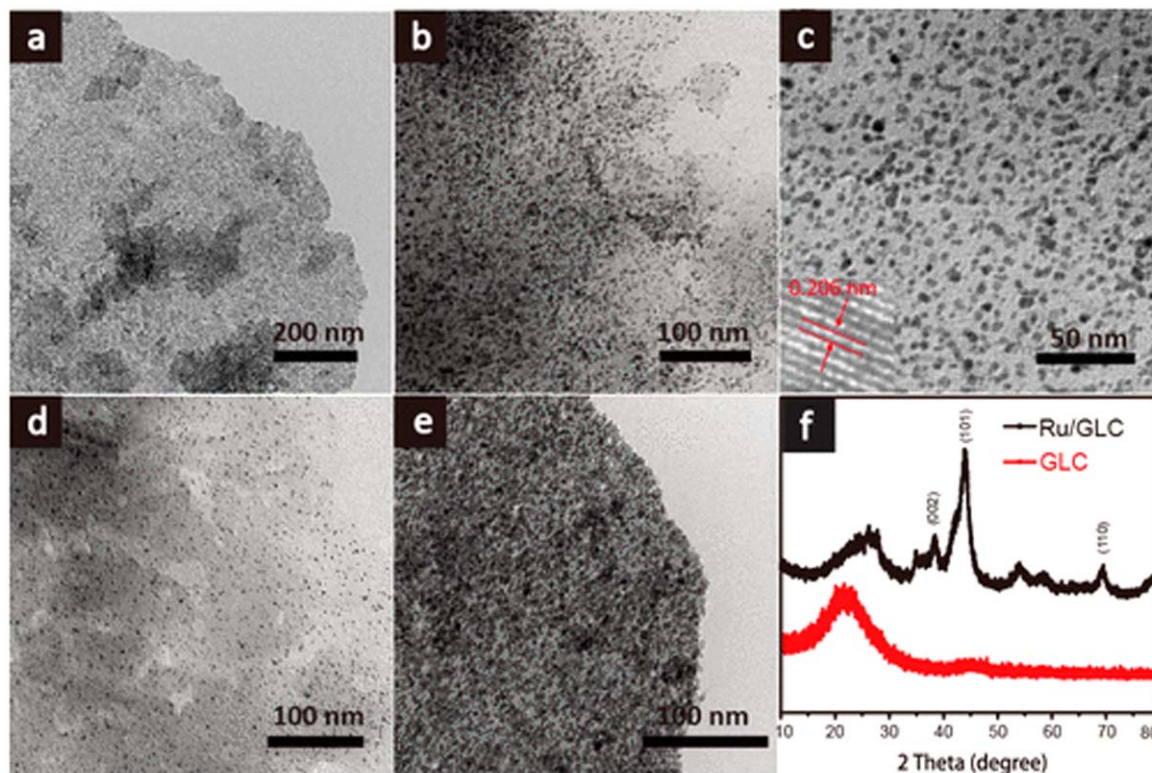

Figure 5. (a)–(c) TEM image of 10 wt.% Ru/GLC; inset in panel c is the HRTEM image of a single Ru nanoparticle. (d) TEM image of 2 wt.% Ru/GLC. (e) TEM image of 62 wt.% Ru/GLC. (f) XRD patterns of GLC and 10 wt% Ru/GLC. Reprinted with permission from Ref. 111. Copyright © 2016, American Chemical Society.
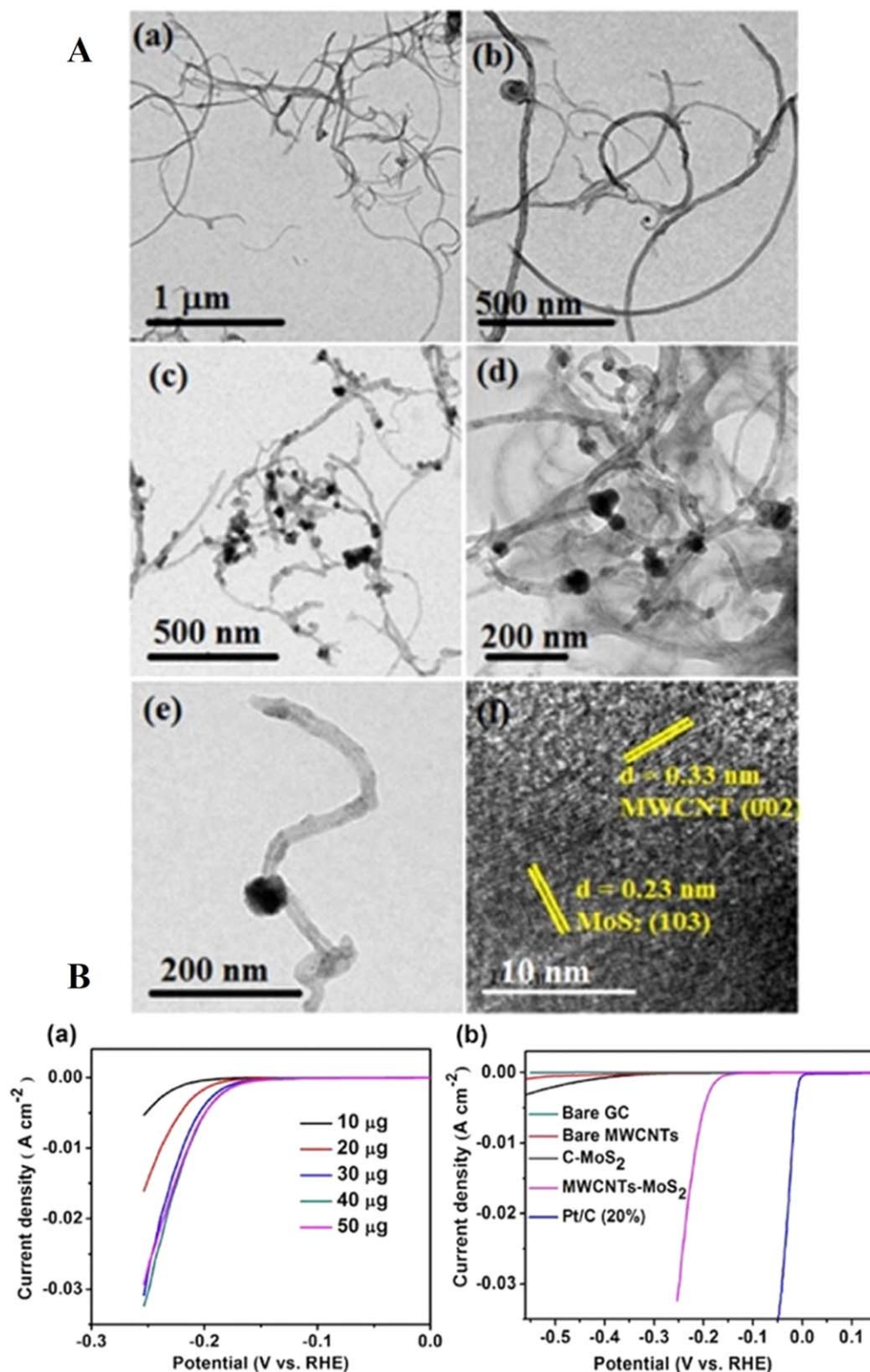
Figure 6. (A) HR-TEM images of (a), (b) bare MWCNTs and (c)–(f) MWCNTs-MoS$_2$ composite. (B) (a) LSV Polarization curves of MWCNTs-MoS$_2$ electrocatalyst with different weight loadings and (b) Comparison of LSV Polarization curves for bare GC, MWCNTs, C–MoS$_2$, MWCNTs-MoS$_2$ and 20 wt. % Pt/C on GC electrode in nitrogen purged 0.5 M H$_2$SO$_4$ at a scan rate of 2 mV s^{-1}. Reprinted with permission from Ref. 112. Copyright © 2017 Wiley-VCH.

density and facile storage.[123] Because of the reasons stated above, electroreduction of CO$_2$ is attracting a lot of interest from the researchers in the last decades.[124–131] Recently there are also some efforts to extend the SCD technology to preparation of highly active

CO$_2$ electroreduction electrocatalysts. Rincon's group had investi-gated MWCNT supported Pt and Pd electrocatalysts prepared via SCD for CO$_2$ electrolyzers.[132,133] Jimenez et al. prepared MWCNT supported Pt or Pb electrocatalysts via SCD at 200 °C and 10 MPa

for 1 h using Pt(acac)$_2$ or lead(II) acetylacetonate (Pb(acac)$_2$) as metal precursors and methanol as co-solvent followed by the in situ reduction introducing H$_2$ (5% H$_2$ in CO$_2$) for 30 min. TEM images showed that Pt nanoparticles were adsorbed onto and into the MWCNTs with a bimodal particle size distributions (3–4 nm and 8–9 nm).[132] This bimodal particle size distribution was attributed to the Pt nanoparticles that were adsorbed and trapped inside the MWCNTs which results in smaller particle size. On the other hand, TEM images of Pb/MWCNTs showed large Pb nanoparticles with 30% of the nanoparticles greater than 100 nm in size attributed to non-optimum conditions in SCD.[133] CO$_2$ electroreduction was performed in PEM-electrolyzer setup where CO$_{2(g)}$ was fed to cathode and 0.1 M potassium bicarbonate (KHCO$_3$) solution was fed to the anode side. Product stream was analyzed via gas chromatography (GC) equipped with flame ionization (FID) and thermal conductivity (TCD) detectors. The effect of current density, temperature and CO$_2$ flowrate to the resulting CO$_2$ conversion and product distribution was investigated. In the case of Pt/MWCNT selectivity values were in the order of formic acid (HCOOH) >methane (CH$_4$)>carbonmonoxide (CO)>methanol (CH$_3$OH). HCOOH was also the major product in the case of Pb/MWCNTs; however, CO production was favored rather than CH$_4$ on Pb/MWCNT. Furthermore, CH$_3$OH selectivity was significantly higher for Pb/MWCNT (6.7%) than Pt/MWCNT (1.9%). Higher hydrocarbon products were also produced in residual amounts. Increasing current density did not influence the selectivity but increased the CO$_2$ conversion for Pt/MWCNT whereas CH$_4$ production increased and CH$_3$OH decreased for Pb/MWCNT. Temperature, conversely, greatly affected the selectivity; mainly at lower temperatures major product was CH$_4$ whereas at high temperatures HCOOH was primarily obtained for Pt/MWCNT. On the other hand, CO became the major product at higher temperatures for Pb/MWCNT with increased CH$_3$OH selectivity. Similarly, low CO$_2$ flowrates promoted the formation of CH$_4$ and CH$_3$OH while at higher flowrates HCOOH formation was favored for Pt/MWCNT while low flowrates promoted the CH$_3$OH formation for Pb/MWCNT. Significant CO$_2$ electroreduction rate was obtained for both Pt/MWCNT and Pb/MWCNT with Pb/MWCNT had 30% lower production rate. On the other hand, carbon supported Cu electrocatalysts showed good activity towards CO$_2$ electroreduction and good selectivity towards CH$_4$ and C$_2$H$_2$.[123,134–137] Carbon supported Cu nanoparticles via SCD were previously reported in the literature[138] but not for the electroreduction of CO$_2$ indicating the need for further research in this area.

Li-ion battery applications.—With the increasing penetration of Li-ion batteries into electric vehicles, research efforts are directed to improve the performance and stability of the Li-ion batteries. SCD may lead to development of exciting materials in this area as demonstrated by Wang et al.[139] They deposited Fe$_3$O$_4$ nanoparticles on hierarchical porous carbon (3DHPC) via SCD and investigated the Li storage capacity. SCD experiments were conducted at 200 °C and 20 MPa for 2 h with the aid of a co-solvent (alcohol was not specified) to dissolve iron (III) nitrate nonahydrate (Fe(NO$_3$)$_3$.9H$_2$O) precursor which was known to be insoluble in scCO$_2$. Fe precursor was converted at 550 °C under flowing N$_2$ for 3 h. SEM and TEM images showed that Fe$_3$O$_4$ was coated uniformly on 3DHPC without any free nanoparticles in scCO$_2$ whereas in pure ethanol most of the formed nanoparticles could not be attached to the surface of the support signifying the efficiency of SCD. Furthermore, the Fe$_3$O$_4$ nanoparticle sizes were between 11 and 15 nm with uniform dispersion with SCD. On the other hand, aggregates were formed on 3DHPC when preparation medium was liquid ethanol. Cyclic voltammograms of Fe$_3$O$_4$/3DHPC prepared via SCD, liquid ethanol and commercial Fe$_3$O$_4$ showed that Fe$_3$O$_4$/3DHPC prepared via SCD had better electrochemical performance than the others. The lithium storage capacity of Fe$_3$O$_4$/3DHPC prepared via SCD was determined as 1768 mA h g^{-1} at initial discharge with the reversible capacity of 1076 mA h g^{-1} which corresponds to 39% irreversible loss in capacity. Furthermore, Fe$_3$O$_4$/3DHPC prepared via SCD

showed excellent stability with continuous cycling. These values were significantly higher than that of Fe$_3$O$_4$/3DHPC prepared via liquid ethanol and commercial Fe$_3$O$_4$ indicating that SCD is a viable method for the preparation of electrocatalysts for Li-ion batteries.

Carbon supported multi-metallic nanoparticles.—Multi-metallic nanoparticles are nanoparticles composed of at least two different metals. Multi-metallic nanoparticles are of both academic and industrial interest as their properties are often different from pure nanoparticles. Similar to bulk alloys, multi-metallic nanoparticles exhibit a very wide range of combinations and compositions. Supported multi-metallic nanoparticles can be used to enhance the performance and for economic reasons. The activity of bimetallic nanoparticles depends on the metal concentration, morphology, and atomic ordering. In multi-metallic nanoparticles, the intrinsic catalytic activity adjustment originates from two cumulative phenomena called the ligand and the strain effect. The addition of another metal causing alteration in the electron density of the system (ligand effect) and the metal–metal bond length change (strain effect) may lead to improved catalytic activity.[140,141] The incorporation of a second metal into the structure may also prevent the poisoning of the catalyst and prolong its aging behavior.[142,143] Synergetic electronic effects towards catalytic reactions can also be significant in alloy or core-shell nanoparticles via the introduction of a change in the d-band center of the metal via the addition of second metal.[144,145] Good examples of these phenomena are highest intrinsic activity of Pt$_3$Ni[146] and dealloyed PtCu$_3$[147] as compared to pure Pt towards the ORR.

Using the SCD technique, Lin et al. prepared bimetallic PtRu with particle sizes around 5–10 nm on the surface of CNTs using simultaneous SCD as electrocatalysts for methanol electrooxidation.[148] The metal precursors (Pt(acac)$_2$ and ruthenium (III) acetylacetone (Ru(acac)$_2$)) were dissolved in scCO$_2$ at 200 °C and 8 MPa along with a small amount of methanol. Then the H$_2$ and CO$_2$ mixture was feed into the vessel which increased the pressure up to 20 MPa. Precursor conversion took 15 min. Electrocatalysts showed promising activity for methanol electrooxidation, which was demonstrated by electrochemical studies including CV, LSV and chronoamperometry. The higher I$_f$ /I$_b$ value and lower onset potential for methanol oxidation showed that the PtRu/CNT exhibited higher activity than that of the Pt/CNT (also synthesized using SCD). The authors suggested that Ru promoted the oxidation of the strongly bound adsorbed CO on Pt by supplying an oxygen source (adsorbed Ru-OH) as proposed in the literature.[149] The high catalytic activity was attributed to the large surface area of CNT and the decrease of the overpotential for methanol electrooxidation. PtRu electrocatalyst was more stable than the Pt electrocatalyst. In the work of Yen et al., electrochemical activities of the 5 different binary metal supported electrocatalysts were investigated.[150] The simultaneous SCD was similar to that of the Lin et al.[148] except for the initial scCO$_2$ pressure (10 MPa) and the pressure after the injection of H$_2$ and CO$_2$ mixture (20 MPa). In this case, the reduction was carried out for 30 min. PtRu catalyst had the highest activity towards methanol oxidation over other bimetallic catalysts and furthermore, it had a forward peak potential of 913 mV (vs. NHE) and a forward peak current of 0.68 A mg$_{Pt}$$^{-1}$. The MWCNT supported bimetallic nanoparticle catalysts all exhibited at least 60% higher I$_f$ /I$_b$ ratios relative to that of Pt monometallic nanoparticles (I$_f$/I$_b$ = 1.4).

An et al. also prepared PtRu/CNT electrocatalysts by SCD for use in DMFCs with different metal precursors (H$_2$PtCl$_6$.6H$_2$O and RuCl$_3$.3H$_2$O) than that of the Wai's group (Pt(acac)$_2$ and Ru(acac)$_2$).[151] The synthesis medium was a CO$_2$-methanol-water solution at high pressure. In order to dissolve the water-soluble precursors in scCO$_2$, methanol and water were used. Adsorption was carried out at 120 °C. After the depressurization, the dark precipitate was separated by centrifugation and washed with ethanol and water and then vacuum-dried at 60 °C for 6 h. Characterization of PtRu/MWCNT composites synthesized with an initial weight ratio of RuCl$_3$. 3H$_2$O:H$_2$PtCl$_6$. 6H$_2$O: MWCNTs at 1:2:2 under an initial CO$_2$ pressure of 6.5 MPa showed that nanoparticles with sizes of

around 5 nm were uniformly dispersed on MWCNTs. An et al. also showed that the produced Pt-Ru/MWCNT composites had high electrocatalytic activities for methanol elctrooxidation. However, they found that the Pt-Ru electrocatalyst was not stable during methanol oxidation reaction for a long time which was attributed to the leaching of ruthenium from the nanocomposite during the reaction.

Erkey's group prepared bimetallic (PtPd/CB) electrocatalysts for PEMFCs by sequential scCO$_2$ deposition.[152] Their sequence consisted of the adsorption/conversion of the first metal (Pt) which was followed by the adsorption/conversion of the second metal (Pd) onto the CB. Nanoparticles with Pd:Pt mole ratios varying between 2:1 and 1:4 were synthesized on CB. The prepared electrocatalyst was rich in Pt for the small nanoparticles (1–4 nm) and Pd rich for larger particles (>5 nm). The ORR activities of the prepared catalysts before potential cycling decreased in the order of: PtPd/BP2000 (1:4) <Pt/BP2000 <PtPd/BP2000 (2:1) < PtPd/BP2000 (1:2) up to approximately 0.5 V (vs. NHE). At 0.7 V (vs. NHE), the worst performance was obtained for Pt/BP2000 catalyst and the activities of the PtPd/BP2000 (1:4) and PtPd/BP2000 (1:2) catalysts became similar. After potential cycling, the order of ORR activity was the same up to 0.35 V (vs. NHE). The activities of the PtPd/BP2000 (1:4) and PtPd/BP2000 (1:2) catalysts became nearly identical over 0.6 V (vs. NHE). The general trends in activity were similar before and after potential cycling, but similar activities were observed at lower potentials which may be attributed to the activity loss of the catalysts with respect to the change in the composition that affects the system negatively. PtPd/BP2000 (2:1) catalyst was absent in terms of single Pd nanoparticles and a large reduction in the Pd content of the PtPd/BP2000 (1:4) catalyst was observed when subjected to potential cycling between 0.6 and 1.2 V (vs NHE). However, after potential cycling, the activity of PtPd/BP2000 (2:1) catalyst was found to be significantly higher due to the dissolution of Pd leaving only Pt nanoparticles on BP2000. Electrochemical measurements also showed the decline of the ESA for the prepared electrocatalysts, but the decline was less pronounced for the Pt rich ones (29% of the ESA after 300 potential cycles of the CVs for the H$_2$ oxidation reaction). They also found from the post-potential cycling tests that the potential losses increased with increasing Pd content in the electrocatalysts.

Barim et al. prepared bimetallic PtCu nanoparticles supported on CA, PtCu/CA via sequential SCD using scCO$_2$ followed by annealing and electrochemical dealloying as electrocatalysts for the ORR.[153] They studied the effect of adsorption order (either Pt or Cu first), Pt:Cu mole ratios, and annealing temperature on the physical properties of the composite nanoparticles. Pt(cod)me$_2$ and Cu(tfa)$_2$ precursors were adsorbed sequentially on the surface of CAsin presence of scCO$_2$ at 35 °C and 10.7 MPa. In order to obtain desired metal uptake and Pt:Cu ratios, single metal adsorption isotherms for the metal precursor-CA systems in scCO$_2$ were used. Bimetallic PtCu deposited CAs were annealed at different temperatures for the conversion of metal precursor to its metal form. XRD and TEM EDXS analyses showed that all samples had disordered PtCu alloy nanoparticles dispersed homogenously on the CA with increase in alloyed PtCu amount with increasing annealing temperature. Average PtCu alloy nanoparticle size was increased with increasing annealing temperature in the range of 1.8 and 4.5 nm with remarkable uniform distribution on CA. Electrochemical characterization was done using CV in 0.1 M HClO$_4$. Prior to electrochemical activity tests, electrocatalysts were dealloyed by continuous cycling in which ORR-inactive excess Cu was selectively leached out of the PtCu nanoparticles in order to create Pt-shell over a PtCu. Authors reported that adsorption order significantly affected the electrochemical performance as first Cu adsorbed samples showed very low activity whereas first Pt adsorbed samples were highly active towards ORR due to differences nanoparticle morphology upon dealloying (Fig. 7). Optimum annealing temperature was determined as 800 °C on the basis of decreased mass activity with higher annealing temperature. Furthermore, electrocatalytic performance

increased with increasing Pt:Cu mole ratio from 1:1 to 1:3 consistent with the earlier reports on similar systems.[154,155] Electrocatalytic activities of the PtCu/CA samples were also compared with the commercial Pt/C and higher ESA and mass activity (at 0.85 V vs. NHE) was obtained with the PtCu/CA sample with Pt:Cu mole ratio 1:3 and annealed at 800 °C as 137 m^2 g^{-1} and 0.123 A mg$_{Pt}$$^{-1}$ indicating that synergistic effects of PtCu/CA.[14]

Recently, CA and Vulcan supported PtCu electrocatalysts were prepared using the simultaneous and sequential in situ supercritical deposition (SCD) method in supercritical CO$_2$ followed by thermal annealing and electrochemical dealloying.[156] Before dealloying, annealed electrocatalysts prepared by simultaneous SCD had a more uniform PtCu composition in PtCu nanoparticles whereas electrocatalysts prepared by sequential SCD led to PtCu nanoparticles with Cu enrichment on the surface. Upon dealloying, PtCu/CA electrocatalyst prepared by simultaneous SCD had an enhanced ESA of 159.4 m^2 g^{-1} due to the synergistic effects of PtCu nanoparticle size and PtCu composition in nanoparticles. All dealloyed electrocatalysts had higher mass activities and PtCu/Vulcan electrocatalyst prepared by simultaneous SCD had the highest mass activity of 0.178 A mg$_{Pt}$$^{-1}$ which was more than twice of the mass activity of commercial Pt/C. PtCu/Vulcan electrocatalyst prepared by sequential SCD showed a specific activity of 0.511 mA cm^{-2} which was 5 times higher than the specific activity of commercial Pt/C.

Zhou et al. prepared 3D honeycomb-structured graphene (HSG) supported PtFe nanoparticles as electrocatalysts for ORR.[49] In a typical synthesis of PtFe/HSG catalyst (Pt: Fe atomic ratio: 40: 60, Pt loading: 11 wt%), HSG powder (5 mg), Pt(hfa)$_2$ (7.1 mg) and Fe(acac)$_2$ (2.9 mg) were loaded into a glass cell. The glass cell with metal precursors was put into a high-pressure stainless-steel reactor (10 ml) located on a heater. 500 ml tetrahydrofuran (THF) was injected into the vessel to modify the polarity of CO$_2$ and to enable dissolution of the metal precursors as a modifier. Then, the reactor was heated to and maintained at 60 °C which made the pressure increase to 30 MPa. After 2 h of adsorption, the vessel was vented. The reduction of the precursors was carried out using a mixture of borane-THF in scCO$_2$ at 80 °C for 30 min followed by depressurization at 50 °C and washing the sample with a continuous feed of scCO$_2$ and final depressurization. Fcc disordered PtFe alloy formation on HSG was observed according the XRD peak shifts with smaller particle sizes (1.4–2.5 nm) as compared to that of the single Pt/HSG sample (4.6 nm). After electrochemical dealloying of Fe from Pt$_{40}$Fe$_{60}$/HSG, the resultant sample showed a significant enhancement in electrocatalytic performance for the ORR, including a factor of 14.2 enhancement in mass activity (1.70 A mg$_{Pt}$$^{-1}$), a factor of 11.9 enhancement in specific activity (1.55 mA cm^{-2}), and higher durability compared with that of Pt/C catalyst (Fig. 8).

Zhou et al. also reported the synthesis of PtFe and PtFeCo nanoparticles supported on graphene cellular monolith (GCM) aerogels as electrocatalysts for the ORR.[157] Samples were prepared in a similar fashion to [49] but this time with a GCM alcogel as starting material. The adsorption and alcogel drying was carried out at the same time. The alcohol contained in the pores of the alcogel also served as entrainers for the dissolution of platinum (II) hexafluoro acetylacetonate (Pt(hfa)$_2$), cobalt (II) hexafluoro acetylacetonate hydrate (Co(hfa)$_2$xH$_2$O) and iron (III) acetylacetonate (Fe(acac)$_2$) precursors who were adsorbed using simultaneous SCD at 15 MPa and 60 °C in scCO$_2$. Subsequently, the precursor reduction was carried out using borane-THF in scCO$_2$ again as in Ref. [49] After electrochemical dealloying, the resultant PtFe/GCM showed the significant enhancement in ORR activity, including a factor of 8.47 enhancement in mass activity (0.72 A mg$_{Pt}$$^{-1}$), and a factor of 7.67 enhancement in specific activity (0.92 mA cm^{-2}), comparing with those of the commercial Pt/C catalyst (0.085 A mg$_{Pt}$$^{-1}$, 0.12 mA cm^{-2}). Importantly, by introducing the Co, the trimetallic PtFeCo/GCM exhibited the further improved ORR activities (1.28 A mg$_{Pt}$$^{-1}$, 1.80 mA cm^{-2}).

Smirnova et al. prepared ternary PtIrCo/CA for methanol and oxygen oxidation reactions.[16] Three organometallic precursors,
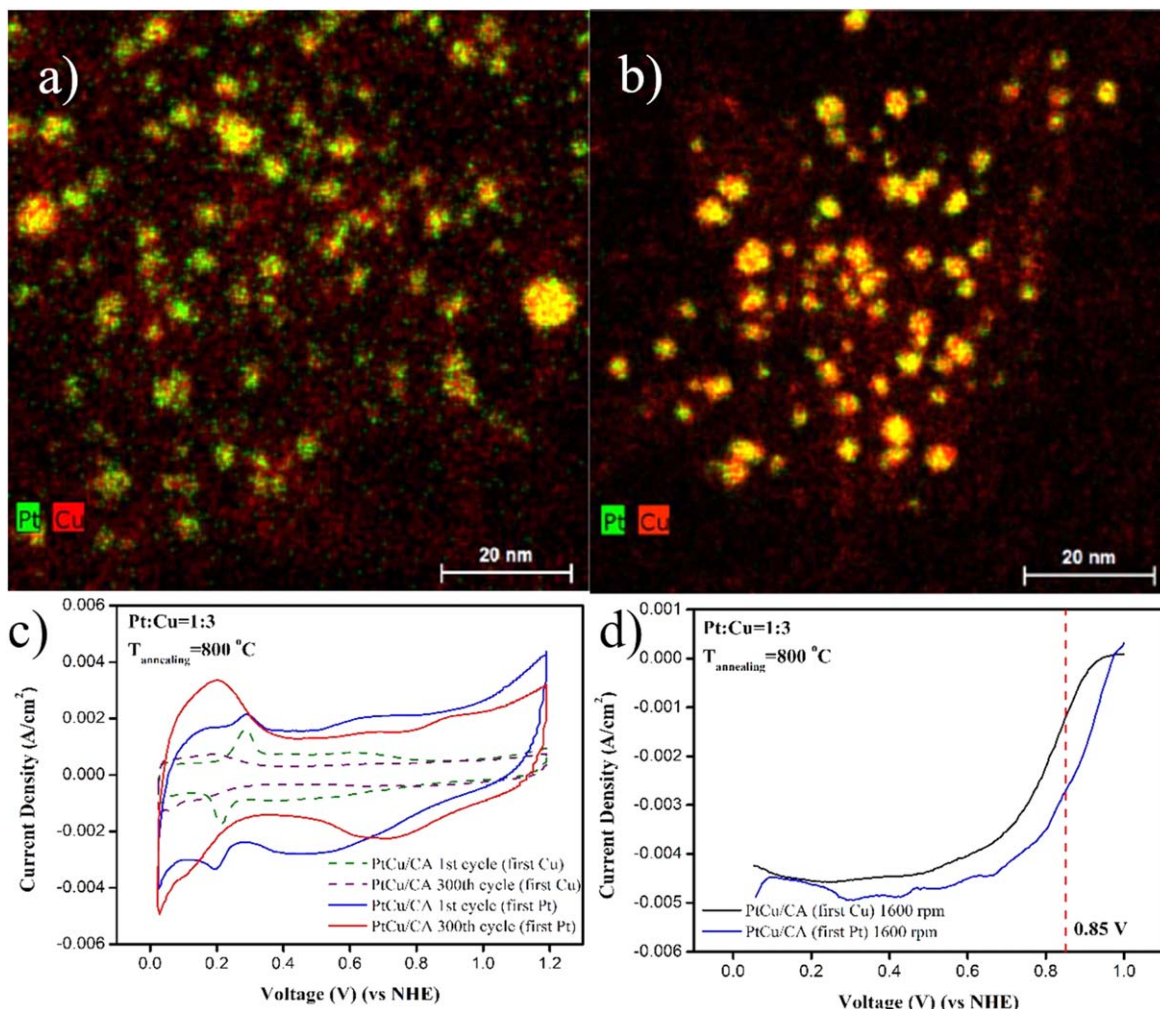
Figure 7. EDX mapping of PtCu/CA samples having Pt:Cu molar ratios of 1:3 prepared using sequential SCD annealed at 800 °C with different deposition orders (a) First Cu, Second, Pt (b) First Pt, Second Cu (c) Cyclic voltammograms of PtCu/CA samples having Pt:Cu molar ratios of 1:3 taken in N_2 saturated 0.1 M $HClO_4$ electrolyte with a scan rate of 50 mV s^{-1}. (d) ORR curves of PtCu/CA samples having Pt:Cu molar ratios of 1:3 taken after electrochemical dealloying in O_2 saturated 0.1 M $HClO_4$ electrolyte with a scan rate of 10 mV s^{-1} and a rotation speed of 1600 rpm. Reprinted with permission from Ref. 14. Copyright © 2018, Elsevier.

Pt(cod)(me)$_2$, methylcyclopentadienyl-(1,5 cyclooctadiene) iridium (I) and cobalt (II) hexafluoro-2,4-pentanedionate hydrate in 2:2:1 ratio together with mesoporous CA were placed inside a stainless-steel vessel followed by charging the vessel with CO_2. Supercritical conditions were reached by increasing the temperature and pressure up to 82 °C and 20 MPa, respectively. As a result, the organometallic precursors were dissolved in scCO_2 and adsorbed within a CA matrix under stirring for 48 h at constant temperature and pressure. Depending on the heat treatment temperature (600 °C or 900 °C), the amorphous organometallic phase of Pt, Ir and Co was transformed into a single-phase fcc PtIrCo-alloy nanoparticles with a mean particle size of 1.7 nm and 2.7 nm, respectively. According to the XRD, the fcc lattice parameters of the PtIrCo-alloy (0.389 nm at 600 °C and 0.386 nm at 900 °C) were smaller than that of the Pt fcc lattice (0.392 nm) and the lattice parameters reduced proportionally to the heat-treatment temperatures. HRTEM results showed uniformly sized PtIrCo nanoparticles. After 50 electrochemical cycles, PtIrCo/CA catalysts displayed improved specific activity (2.5 X Pt/ C), mass activity (3 X Pt/C) at 0.7 V (vs SHE), higher CO-tolerance, and better electrochemical stability than Pt/C, but less CO-tolerance and stability than PtRu/C for methanol electrooxidation. Regarding ORR, the PtIrCo/CA catalysts demonstrated enhanced ORR specific activity (5.5 X Pt/C) and mass activity (6.3 X Pt/C) at 0.7 V (vs. SHE) along with superior methanol-tolerance in comparison to Pt/C.

Polymer supported nanoparticles.—scCO_2 displays high permeation rate in many polymers and the exposure to scCO_2 results in various extents of swelling. This is particularly advantageous for the synthesis or processing of polymer nanocomposites as well as for impregnating a wide variety of chemicals into various polymers. Moreover, the degree of CO_2 sorption/swelling in polymers, diffusion rates within the substrate, and the partitioning of solutes between the SCF and the swollen polymer can be tuned by density mediated adjustments of solvent strength via changes in temperature and pressure. The weight fraction of CO_2 inside the polymer increases appreciably with increasing pressure. The effect of temperature on CO_2 sorption is more complex; until a certain percent of CO_2 sorbs inside the polymer, the sorption of CO_2 increases with decreasing temperature at a particular pressure then increases with increasing temperature. The effect of temperature on CO_2 sorption also exhibits a cross-over due to the reach of critical concentration where the glass transition occurs. On the other hand, high pressure CO_2 can also plasticize polymers as it sorbs in them.[158–165]

In 1995, a SCF was first successfully employed by Watkins et al. for the preparation of polymer supported Pt nanoparticles.[159] Pt(cod)me$_2$ was adsorbed into poly(4-methylpent-1-ene) (PMP) and poly(tetrafluoroethylene) (PTFE) assisted by scCO_2 at 80 °C and 15.5 MPa for 4 h. The precursor was reduced by (i)
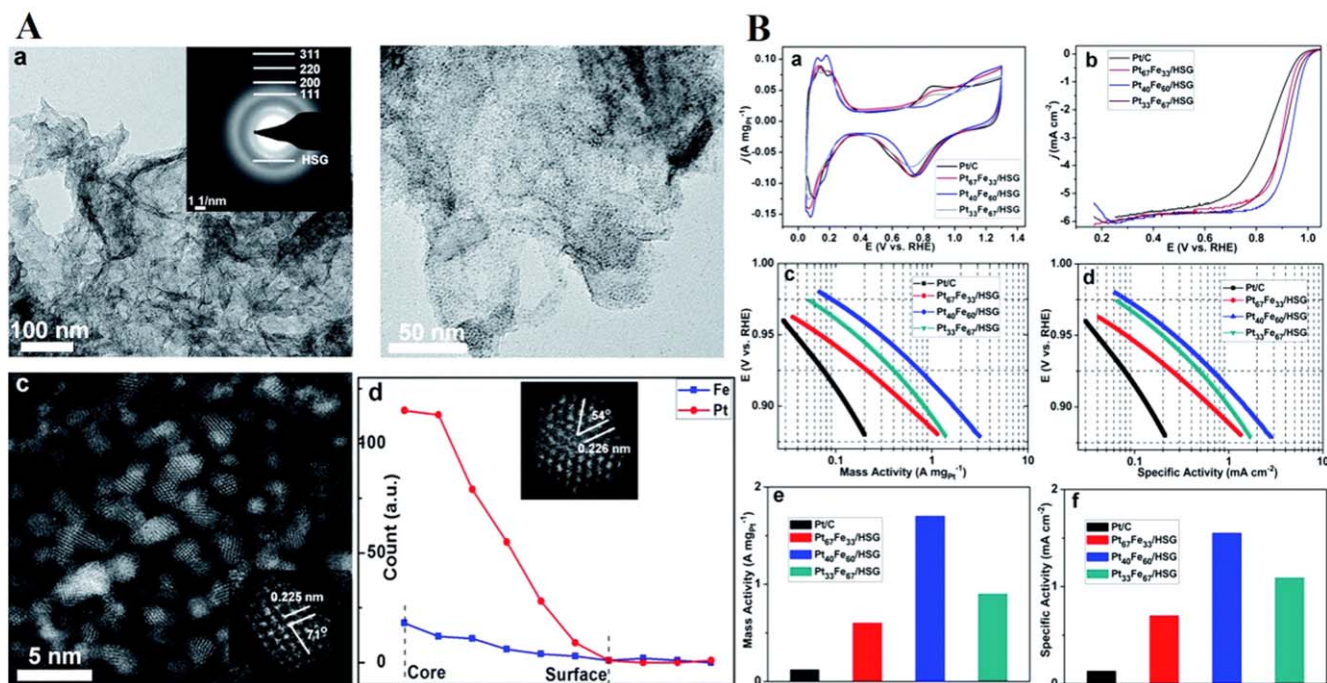
Figure 8. (A) TEM images of (a and b) $Pt_{40}Fe_{60}$/HSG-2 with high Pt-loading of 23 wt%, inset in (a) is selected area electron diffraction pattern (EDP) image. (c) HAADF-STEM image of initial $Pt_{40}Fe_{60}$ NPs (c) and de-alloyed $Pt_{40}Fe_{60}$ NP (inset in d). HAADF-STEM image shows the initial and de-alloyed NPs have good crystallinity with fcc structure. Insets are enlarged NPs with annotations of {111} planes and angles consistent with fcc structures. (d) EDX-line scan profile across an individual de-alloyed $Pt_{40}Fe_{60}$ NPs. (B) Electrochemical properties of PtFe/HSG catalysts. (a) CVs and (b) ORR polarization curves of commercial Pt/C, $Pt_{67}Fe_{33}$/HSG, $Pt_{40}Fe_{60}$/HSG and $Pt_{33}Fe_{67}$/HSG catalysts. (c) and (d) The corresponding Tafel plots. (e) Mass activities and (f) specific activities measured at 0.9 V. Reprinted with permission from Ref. 49. Copyright © 2016, The Royal Society of Chemistry.

hydrogenolysis (24 h) subsequent to depressurization at 60 °C and 7 MPa of H_2, (ii) hydrogenolysis (4 h) in CO_2 at 80 °C and 15.5 MPa induced by the addition of a ~10-fold excess of H_2 to the reaction vessel prior to depressurization, and (iii) thermolysis (20 h) in CO_2 induced by raising the temperature to 140 °C prior to decompression (final pressure ~26.5 MPa). TEM images of Pt/PMP synthesized by methods (i) and (ii) indicated the presence of discrete Pt clusters in PMP having a maximum nanoparticle size of approximately 15 nm for method (i) and 50 nm for method (ii), respectively.

For the Pt/PMP composites synthesized by method (ii), SEM images of the composite cross section revealed a sharp concentration gradient between a Pt-enriched surface layer and the bulk of the substrate which contained a uniform concentration of the <50 nm Pt particles. A high concentration of larger platinum crystals (50–100 nm) was observed. TEM images of thermal reduction of the precursor in CO_2-swollen PMP at 140 °C revealed feathery platinum aggregates comprised of smaller primary particles. The aggregates, which were distributed throughout the substrate, had a maximum size of approximately 50 nm.

Quite a few more studies have been conducted since then metallic nanoparticles of Au, Ag, Pt and Pd have been incorporated into a wide variety of polymers using SCD.[166–168]

Pd-impregnated Nafion® membranes were synthesized via SCD for the first time by Erkey's group,[166] which involved impregnation of Nafion® membranes with $Pd_2(hfa)_2$ from scCO2 solution followed by subjecting the impregnated membrane to H_2. The adsorption was carried out at 80 °C and 13.6 MPa for 12 h. The conversion of the precursor to the metal form was carried out in situ by injecting H_2 into the vessel at high pressure and keeping at these conditions for 8 h. The resulting membranes had Pd loadings of 1.19 and 2.65 m cm^{-2}. According to SEM images, the membrane had a uniform surface morphology and no cracks could be observed. TEM image of the cross-section of the composite membrane indicated a thin (0.3 μm) film of Pd around the membrane surface and a significant number of isolated Pd nanoparticles deeper in the membrane

(Figs. 9a and 9b). The particle size of the Pd nanoparticles ranged from 5 to 10 nm. MEAs using these palladinized Nafion® membranes were prepared and evaluated in DMFCs to determine methanol cross-over, proton conductivity as well as DMFC performance. The Pd-impregnated Nafion® membranes showed reduced methanol cross-over and gave higher cell performance than that of pure Nafion® membrane, although the proton conductivity was decreased with the incorporation of Pd. The palladinized membrane showed more significant benefits in performance with higher concentration (5 M) of methanol. (Fig. 9c)

Later, Zhang et al. prepared Pt-carbon black-Nafion® 112 and Pt-Nafion® 112 composites in scCO2 by adsorbing $Pt(cod)me_2$ precursor on the CB-Nafion® 112 composite at 80 °C and 27.6 MPa for 24 h followed by the ex situ conversion at 200 °C under flowing N_2 for 2 h.[167] Thermogravimetric analysis (TGA) was conducted in order to ensure that Nafion® 112 was not decomposed during adsorption and conversion. TGA of blank Nafion® 112 did not show significant decomposition until 240 °C, therefore, Pt-CB-Nafion® 112 composites could be prepared at chosen adsorption and conversion conditions. Fourier Transform Infra-red Spectroscopy (FTIR) of $Pt(cod)me_2$, Nafion® 112, $Pt(cod)me_2$- Nafion® 112 and Pt-Nafion® 112 composites showed that $Pt(cod)me_2$ was successfully adsorbed on Nafion® 112 and converted without any significant degradation to Nafion® 112 structure. Furthermore, water peaks were also seen in the FTIR spectra indicating that water adsorbent nature of Nafion® 112 was preserved after thermal treatment. Average Pt nanoparticle size was determined from H_2 chemisorption as 2.6 nm. Cyclic voltammograms of Pt-carbon black- Nafion® 112 composite was taken in a single-cell fuel cell setup. ESA was determined as 20 m^2 g^{-1}. Authors suggested that in situ conversion with H_2 can result in better dispersion due to low temperature in scCO2.

Using the same technique, Kim et al. investigated the incorporation of Pd nanoparticles onto Nafion® 117 membranes.[168] The membranes were impregnated with palladium (II) acetylacetonate ($Pd(acac)_2$) at 20 MPa and 80 °C for 4 h in scCO2 followed by
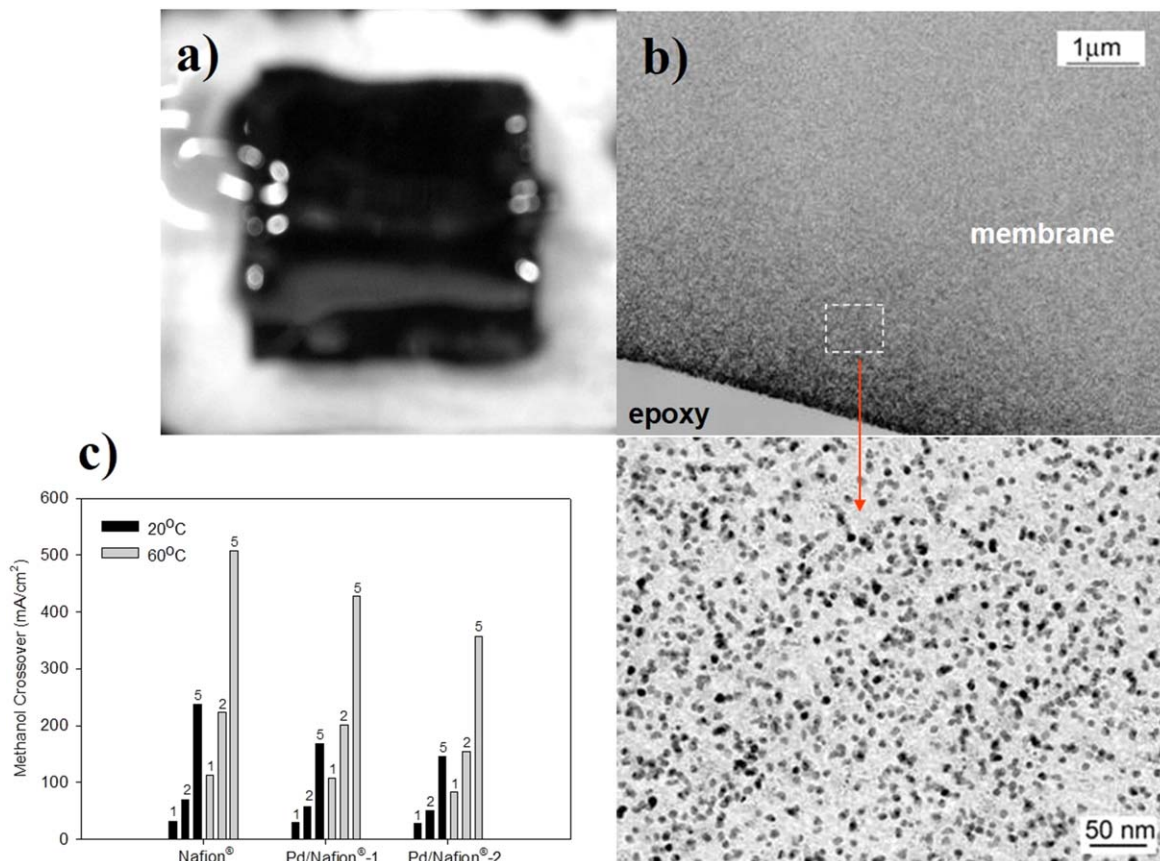
Figure 9. (a) Membrane appearance (b) TEM images of the partial cross section of a Pd-impregnated Nafion® 117 membrane (Pd/Nafion®-2, with 1.05 mg cm⁻² Pd loading on Nafion® 117) (c) Methanol crossover performances of Pd/Nafion® 117 composites. Reprinted with permission from Ref. 166. Copyright © 2005, The Electrochemical Society.

chemical decomposition. The results indicate that the Pd/Nafion® composite membranes showed different morphologies depending on the concentration of the reducing agent (NaBH₄) in the injected solution. They obtained Pd nanoparticles of 4–5 nm using a 0.5 mM solution of NaBH₄, whereas for 10 and 100 mM solutions, the average diameter of the nanoparticles was 20–70 nm. They observed that the ion conductivity of Pd/Nafion® reduced using a 0.5 mM (0.0833 s cm⁻¹) NaBH₄ solution was higher than that of the Nafion® 117 (0.0740 s cm⁻¹). However, the increase of the reducing agent concentration led to a decrease in the ion conductivity to a level even less than that of the Nafion® 117 which was attributed to the increase of the Pd nanoparticle size. It was suggested that the ability of the nanoparticles with sizes in the range of 20–70 nm to conduct protons were less than that of 4–5 nm sized nanoparticles. Additionally, the permeability of the composite membranes decreased with the increasing NaBH₄ concentration. They also tested the composite membranes in a DMFC with 2 M methanol at 80 °C with air in the cathode. As a result of the competition phenomenon between the ionic conductivity (0.0765 s cm⁻¹) and permeation rate (4.38 × 10⁻⁷ cm² s⁻¹), the composite membranes prepared using 2 mM reducing agent had the best cell performance and 44% higher current density than that of Nafion® 117.

Thin films.—Thin films constitute an important functional structure family for electrochemical devices. The most common thin film deposition techniques are chemical vapor deposition (CVD) and aqueous electrochemical deposition (electroplating and electroless plating). Major limitations of CVD include the volatility requirement of the organic precursor and the elevated deposition temperatures that can produce toxic radicals, cause thermal stress in the deposited films, and hinder the use of labile materials as substrates, such as polymers. Even though the aqueous electrochemical deposition methods are solution-based techniques carried out at lower temperatures, they suffer from aqueous waste with possible heavy metal contamination, sluggish deposition kinetics, and poor control over the deposition rate and conformity. To address these issues, SCD of thin films was developed by Watkins and coworkers.[169,170] Starting with Pd and Pt thin films, the technique is now extended by Watkins as well as other researchers to form thin films of various metals, metal alloys, metal oxides, metal sulfides, semiconductors, polymers, composite materials, and so on (Concise review of these SCD applications can be found in Refs. 1–4, 171–173). SCD is shown to have various advantages over conventional thin film deposition techniques. Since SCD is essentially a solution-based technique in which the solvating power of the fluid can be adjusted by density, volatility of the metal precursors is not an indispensable requirement. Similarly, most common reducing agents such as H₂ and alcohols are soluble in the supercritical fluids. The deposition can be carried out at lower temperatures than CVD, a feature of SCD that expands the range of materials that can be used as substrates, eliminating generation of toxic radicals, and alleviating the thermal stress in the deposited films. Despite liquid-like densities, the favorable gas-like transport properties of supercritical fluids, such as orders-of-magnitude lower viscosity and orders-of-magnitude higher diffusivity than liquids combined with zero surface tension, facilitate conformal deposition of thin films in confined geometries with high aspect ratios. In the literature, thin film SCD is mostly used for microelectronic applications.[173,174] Here, we restrict the discussion of literature to only the articles dealing with SCD of thin films for electrochemical applications in which continuous films layers were deposited and electrochemical characterizations were performed.

In literature, the main thin film SCD applications in fuel cells focus on solid-oxide fuel-cells (SOFCs). Most of the seminal work in the area of SCD of thin films for SOFCs was conducted by Watkins and coworkers.[175–177] Bassat et al. investigated the SCD of undoped ceria (CeO_2) films on top of both sides of yttria-stabilized zirconia (YSZ) electrolytes as a buffer layer to prevent diffusion of cations at cathode-electrolyte interface and to improve mechanical adhesion between YSZ and cathode in low-temperature SOFCs.[175] Using a cold wall reactor where the sample stage temperature was held at 300 °C, dense, continuous, uniform, conformal and crystalline CeO_2 films (20–200 nm) were obtained in short reaction durations (30 min) through the hydrolysis of cerium β-diketonate in humidified $scCO_2$ (the pressure was not reported). The contamination due to precursor decomposition products were seen to be removed after a short annealing step in air at 400 °C. Upon annealing, good mechanical adhesion was observed between the deposited CeO_2 film and YSZ. Although the studied experimental parameters of SCD were limited, it was reported that the most important experimental parameter affecting the film properties was H_2O:Ce precursor molar ratio. Increasing the H_2O:Ce precursor ratio was stated to favor the precursor hydrolysis leading to thicker, smoother and denser films. Interestingly, a consistent trend of decreasing polarization resistance was seen with increasing H_2O:Ce precursor ratio using SCD-employed undoped CeO_2 interlayer. Besides, the polarization resistance values obtained with undoped CeO_2 were similar to those obtained with doped CeO_2. To further explore that finding, the authors focused on the SCD of undoped CeO_2 thin films in their next study.[176] Using the same base procedure as in their previous study, an analysis of influence of SCD parameters, such as precursor concentration, water content, temperature, pressure, deposition time, was performed. No clear effect of decreasing the stage temperature from 300 °C to 250 °C in SCD was observed in the polarization resistance. The change in pressure between 13–28 MPa did not affect the deposited film morphology. Longer deposition time (up to 3 h) was found to solely increase the thickness of the film without changing the film morphology, crystallinity or composition implying fast kinetics of the precursor hydrolysis in film deposition. The previous findings of decrease in polarization resistance and smoother and denser films with high H_2O:Ce precursor ratios were verified in this study as well (Fig. 10). Intriguingly, comparing undoped ceria deposited using SCD on thin (100 μm) and thick (1 mm) YSZ electrolytes, it was reported that the effect of H_2O:Ce precursor ratio on film morphology was not clearly observed in thick YSZ electrolytes. A lower temperature at the surface of the thick electrolyte due to thicker YSZ layer between the heated stage and YSZ surface was argued to be the reason. In short, both studies demonstrated the feasibility and advantages of SCD in preparation of CeO_2 buffer layers for low-to-intermediate temperature SOFCs.

In another study, Le Trequessera et al. investigated the co-deposition of YSZ thin films on Si wafers in a cold wall reactor using $scCO_2$ with 300 °C stage temperature, 60 °C wall temperature and 15–20 MPa pressure for use in micro SOFCs.[177] Both Y and Z precursors were stated to undergo a hydrolysis reaction for yttria and zirconia film formation, respectively. As opposed to a conventional batch co-deposition process, co-deposition of yttria and zirconia was done by employing a cyclic precursor injection for homogeneous film composition (5–6 cycles). Each cycle of the cyclic process included injection of the mixed precursors into $scCO_2$, allowing a short interval for reaction to take place on Si wafer, and then purging of the reactor contents. XPS depth profiles of YSZ films produced using the cyclic process and the conventional batch process were compared for assessing the distribution of elements, thus homogeneity of films, as seen in Fig. 10. At the surface of the sample prepared using batch process (30 min), the atomic concentration of Y was negligible whereas that of Z was high owing to fast hydrolysis of Y precursor than that of Z precursor. A more uniform film composition was observed in the sample prepared using cyclic process (5–6 cycles, 30 min for each cycle) yet with a pseudo-sinusoidal behavior of film composition due to difference of hydrolysis rates of Y and Z precursors. Shorter reaction intervals in the cyclic process (5–6 cycles, 10 min for each cycle) resulted in considerable uniformity improvement in film composition such that the precursor molar ratio (85:15 Zr:Y for precursors) was fully reflected in the stoichiometry of the deposited films (86:14 Zr:Y). Interestingly, it was found that in case where the same amount of water and precursors were used in batch process and in cyclic process (10 min cycles), the cyclic deposition process provided thicker films. This finding was explained by the higher reaction rate in the cyclic process due to refreshed of water concentration in each cycle driving the reaction to the product side (product being the deposited oxide). Besides, the purge at the end of each cycle helped remove the precursor decomposition products avoiding buildup of contaminants. The cyclic process developed in this study can be utilized in cases where precise control of stoichiometry is sought after in SCD.

Do et al. investigated SCD for depositing vanadium pentoxide (V_2O_5) films on MWCNT buckypaper for obtaining binder-free composite electrodes for supercapacitor applications.[178] The buckypaper was a stable network of entangled MWCNTs in the form of a highly porous membrane with a specific surface area of 250 m^2 g^{-1} and a thickness of 80 μm. Using $scCO_2$ at temperatures 50°C–70°C and pressures 13.8–20.7 MPa, a typical vanadium precursor loading of 9 wt% was obtained on the buckypaper. Unlike the other thin film SCD techniques mentioned above, the conversion of the precursor to metal oxide was performed by heating the sample to 300 °C in air for 5 h (ex situ conversion of precursor to metal oxide). SEM, EDS, TEM and wide-angle X-ray scattering (WAXS) results showed uniform deposition of sub-nanometer thick, amorphous V_2O_5 film over the walls of MWCNTs throughout the depth of buckypaper. CV measurements (1 M KCl) of a composite electrode with 6.92 wt%
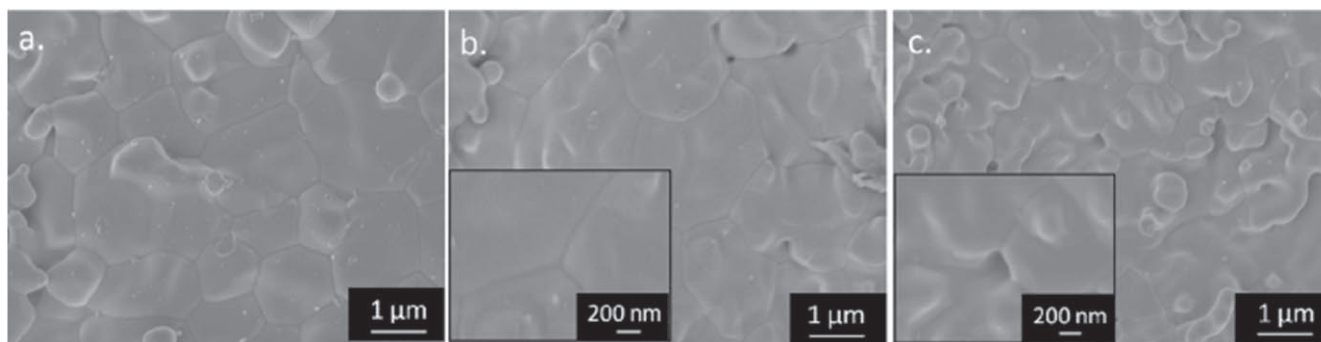

Figure 10. SEM and FEG SEM micrographs of CeO_2 films deposited in $scCO_2$ on YSZ (100 μm) substrate without and with water added: (a) substrate surface, (b), (c) film with H_2O:Ce precursor ratio 0.06, (d)–(f) film with H_2O:Ce precursor ratio 12. Films annealed at 400 °C. Reprinted with permission from Ref. 176. Copyright © 2011, American Chemical Society.
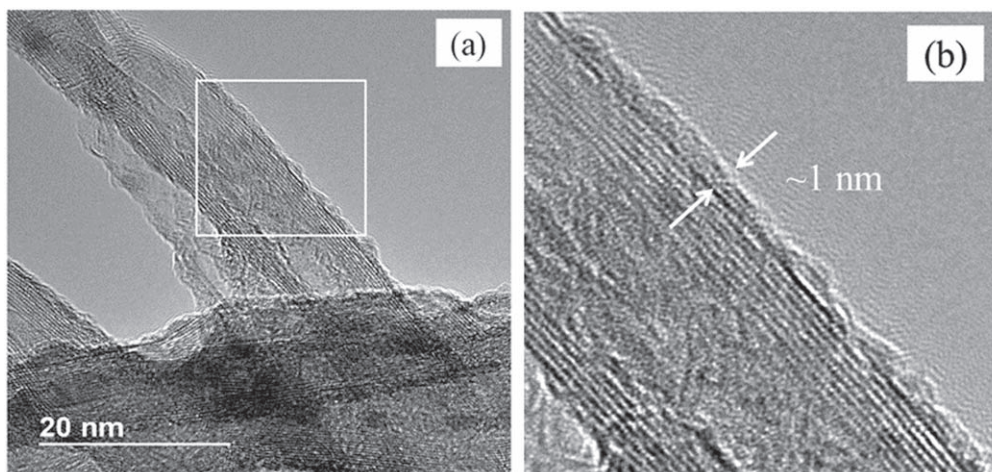
Figure 11. TEM images of composite sample with 50 wt% V_2O_5 after annealing. (b) is the close-up image of the marked region in (a). Reprinted with permission from Ref. 179. Copyright © 2018, American Chemical Society.

V_2O_5 loading showed a specific capacitance of 85 F g^{-1} at 100 mV s^{-1} scan rate which was more than four times of that of pristine buckypaper.

Recently, Do et al. revisited the SCD of V_2O_5 films on buckypaper for composite electrodes of supercapacitors.[179] Unlike their previous studies, they used in situ conversion of vanadium precursor to V_2O_5 by supplying oxygen into the pressure vessel. After SCD, the obtained amorphous V_2O_5 films were converted to crystalline films by annealing in air at 300 °C for 1 h. The resulting samples contained up to 50 wt% V_2O_5. Continuous, uniform, and conformal 1 nm thick V_2O_5 films (about three crystalline atomic layers) on MWCNTs were obtained (Fig. 11). The composite electrodes showed a high specific capacitance of 187 F g^{-1} at 2 mV s^{-1} and 120 F g^{-1} at 100 mV s^{-1} scan rates in 1 M KCl electrolyte. However, an observed stability issue was the dissolution of V_2O_5 in KCl solution after an extended period of time, which was noted to decrease the obtained capacitance values significantly after a few hundred cycles. The authors claimed that this issue can be overcome by using different electrolytes that do not dissolve V_2O_5. In short, SCD was shown to be very effective in obtaining conformal V_2O_5 films on buckypaper yielding improved specific capacitance values in supercapacitors.

Summary and Future Prospects

SCD shows great promise for development of novel functional materials which will aid in widespread usage of electrochemical energy conversion systems. Using SCD, metallic nanoparticles can be incorporated to carbonaceous supports for use as electrocatalysts for fuel cells and electrolyzers or to polymers for use as proton exchange membranes. In most cases, the electrocatalysts prepared by using SCD had higher electrochemical activities than that prepared by conventional techniques. However, the Pt cost needs to be reduced further and bimetallic Pt electrocatalysts such as PtCo/C employed in Toyota Mirai are already playing a very important role in this matter. SCD provides excellent control of particle size, morphology, and composition of bimetallic nanoparticles. The results from a few studies on preparation of bimetallic and multimetallic catalysts using SCD are promising and indicate the need for more detailed investigations on other metal pairs. Further investigations on the binary solubilities of metallic precursors in SCFs as well as the understanding of phase behavior of these mixtures are crucial. Studies are needed especially on determination of binary and ternary adsorption isotherms for metallic precursors between various supports and the scCO$_2$ phase to be able control metal loading and composition. These studies should be coupled with appropriate electrochemical tests to elucidate the effect of morphology on electrochemical activity. Computational studies would also provide very beneficial fundamental information on metal support interactions. Development of cheap electrocatalysts, which do not contain Pt, is another area where SCD can contribute. It has already been demonstrated that SCD can enable synthesis of very active non-PGM electrocatalysts in alkaline media. The ability to utilize SCD with polymers could result in the development of electrolyte-carbon-metal interfaces with very favorable nanoarchitectures for high electrochemical activity. Methanol cross-over, an important challenge encountered in DMFCs, can be reduced by incorporating metal nanoparticles onto the surface of the membranes. The studies on the SCD of thin films for electrochemical applications is currently limited in the literature. In order to expand the range of electrochemical applications in that area, the utilization of SCD of thin films can be investigated in battery, sensor and electrolyzer research. Moreover, computational studies on thermodynamics and kinetics of thin film deposition using SCD can provide fundamental understanding of the underlying mechanisms, predictive capabilities for design of thin film SCD equipment and optimization of thin film SCD process. Application of SCD technology for the atomic layer deposition of thin films is a promising research field in the future. With the recent advancements in the field of SCF technologies for the production of materials such as aerogel blankets and impregnated wood on a commercial scale, SCD to prepare supported metal nanoparticles and films for electrochemical applications has a great potential for application on an industrial scale.

References

1. S. E. Bozbag and C. Erkey, *J. Supercrit. Fluids*, **96**, 298 (2015).
2. S. E. Bozbag, D. Sanli, and C. Erkey, *J. Mater. Sci.*, **47**, 3469 (2012).
3. S. E. Bozbag and C. Erkey, *J. Supercrit. Fluids*, **62**, 1 (2012).
4. D. Sanli, S. E. Bozbag, and C. Erkey, *J. Mater. Sci.*, **47**, 2995 (2012).
5. C. Erkey, in *Supercritical Fluids & Organometallic Compounds* (Elsevier, Amsterdam) (2011).
6. C. Erkey, *J. Supercrit. Fluids*, **47**, 517 (2009).
7. Y. Zhang and C. Erkey, *J. Supercrit. Fluids*, **38**, 252 (2006).
8. S. E. Bozbag and C. Erkey, *J. Supercrit. Fluids*, **62**, 1 (2012).
9. A. H. Romang and J. J. Watkins, *Chem. Rev.*, **110**, 459 (2010).
10. D. Hu, H. Xu, Z. X. Yi, Z. Chen, C. L. Ye, Z. T. Wu, H. F. Garces, and K. Yan, *ACS Sustain. Chem. Eng.*, **7**, 15339 (2019).
11. P. G. Corradini, F. I. Pires, V. A. Paganin, J. Perez, and E. Antolini, *J. Nanopart. Res.*, **14**, 9 (2012).
12. D. V. Pugh, A. Dursun, and S. G. Corcoran, *J. Electrochem. Soc.*, **152**, B455 (2005).
13. Y. Y. Huang, T. S. Zhao, L. Zeng, P. Tan, and J. B. Xu, *Electrochim. Acta*, **190**, 956 (2016).
14. S. B. Barim, S. E. Bozbag, H. B. Yu, R. Kizilel, M. Aindow, and C. Erkey, *Catal. Today*, **310**, 166 (2018).
15. K. S. Morley, P. Licence, P. C. Marr, J. R. Hyde, P. D. Brown, R. Mokaya, Y. Xia, and S. M. Howdle, *J. Mater. Chem.*, **14**, 1212 (2004).
16. P. Kolla and A. Smirnova, *Electrochim. Acta*, **182**, 20 (2015).

17. J. J. Watkins and T. J. McCarthy, *Chem. Mater.*, **7**, 1991 (1995).
18. O. Aschenbrenner, S. Kemper, N. Dahmen, K. Schaber, and E. Dinjus, *J. Supercrit. Fluids*, **41**, 179 (2007).
19. J. A. Darr and M. Poliakoff, *Chem. Rev.*, **99**, 495 (1999).
20. C. Erkey, *J. Supercrit. Fluids*, **17**, 259 (2000).
21. N. G. Smart, T. Carleson, T. Kast, A. A. Clifford, M. D. Burford, and C. M. Wai, *Talanta*, **44**, 137 (1997).
22. M. Skerget, Z. Knez, and M. Knez-Hrncic, *J. Chem. Eng. Data*, **56**, 694 (2011).
23. S. G. Kazarian, M. F. Vincent, F. V. Bright, C. L. Liotta, and C. A. Eckert, *JACS*, **118**, 1729 (1996).
24. T. Casimiro, F. Montilla, S. Garcia, T. Avilés, S. Raeissi, A. Shariati, C. J. Peters, M. Nunes da Ponte, and A. Aguiar-Ricardo, *J. Supercrit. Fluids*, **31**, 1 (2004).
25. D. Liu and D. L. Tomasko, *J. Supercrit. Fluids*, **39**, 416 (2007).
26. J. Chrastil, *J. Phys. Chem.*, **86**, 3016 (1982).
27. A. Niu, Y. J. Han, J. A. Wu, N. Yu, and Q. Xu, *J. Phys. Chem. C*, **114**, 12728 (2010).
28. J. Z. Yin, Q. Q. Xu, and A. Q. Wang, *Chem. Eng. Commun.*, **197**, 627 (2010).
29. M. Alibouri, S. M. Ghoreishi, and H. R. Aghabozorg, *AlChE J.*, **55**, 2665 (2009).
30. C. Aymonier, A. Denis, Y. Roig, M. Iturbe, E. Sellier, S. Marre, F. Cansell, and J. L. Bobet, *J. Supercrit. Fluids*, **53**, 102 (2010).
31. H. Wakayama and Y. Fukushima, *J. Chem. Eng. Jpn.*, **42**, 134 (2009).
32. Z. M. Chen, M. C. Zhuo, F. F. Xue, J. F. Chen, and Q. Xu, *Ind. Eng. Chem. Res.*, **48**, 3441 (2009).
33. S. R. Puniredd, C. M. Yin, Y. S. Hoo, P. S. Lee, and M. P. Srinivasan, *J. Colloid Interface Sci.*, **332**, 505 (2009).
34. S. R. Puniredd, B. C. C. Nguan, and M. P. Srinivasan, *J. Colloid Interface Sci.*, **333**, 679 (2009).
35. G. Aksomaityte, F. Cheng, A. L. Hector, J. R. Hyde, W. Levason, G. Reid, D. C. Smith, J. W. Wilson, and W. Zhang, *Chem. Mater.*, **22**, 4246 (2010).
36. B. I. Lee, D. Bae, J. K. Kang, H. Kim, and S. H. Byeon, *Bull. Korean Chem. Soc.*, **30**, 1701 (2009).
37. G. I. Garrido and F. C. Patcas, A, G. Upper, M. Türk, S. Yilmaz, and B. Kraushaar-Czarnetzki, *Appl. Catal., A*, **338**, 58 (2008).
38. S. Lang, M. Türk, and B. Kraushaar-Czarnetzki, *J. Catal.*, **286**, 78 (2012).
39. B. Cangul, L. C. Zhang, M. Aindow, and C. Erkey, *J. Supercrit. Fluids*, **50**, 82 (2009).
40. S. E. Bozbag, N. S. Yasar, L. C. Zhang, M. Aindow, and C. Erkey, *J. Supercrit. Fluids*, **56**, 105 (2011).
41. C. D. Saquing, T. T. Cheng, M. Aindow, and C. Erkey, *J. Phys. Chem. B*, **108**, 7716 (2004).
42. C. D. Saquing, D. Kang, M. Aindow, and C. Erkey, *Microporous Mesoporous Mater.*, **80**, 11 (2005).
43. Y. Zhang, B. Cangul, Y. Garrabos, and C. Erkey, *J. Supercrit. Fluids*, **44**, 71 (2008).
44. G. Caputo, I. De Marco, and E. Reverchon, *J. Supercrit. Fluids*, **54**, 243 (2010).
45. G. Brunner and M. Johannsen, *J. Supercrit. Fluids*, **38**, 181 (2006).
46. I. Ushiki, N. Takahashi, M. Koike, Y. Sato, S. Takishima, and H. Inomata, *J. Supercrit. Fluids*, **135**, 137 (2018).
47. J. Wang, T. Yu, X. Q. Wang, G. S. Qi, J. J. Xue, M. Q. Shen, and W. Li, *Appl. Catal. B-Environ.*, **127**, 137 (2012).
48. F. E. S. Oztuna, S. B. Barim, S. E. Bozbag, H. B. Yu, M. Aindow, U. Unal, and C. Erkey, *Electrochim. Acta*, **250**, 174 (2017).
49. Y. Z. Zhou, C. H. Yen, Y. H. Hu, C. M. Wang, X. N. Cheng, C. M. Wai, J. Yang, and Y. H. Lin, *J. Mater. Chem. A*, **4**, 18628 (2016).
50. V. N. Bagratashvili, A. O. Rybaltovsky, N. V. Minaev, P. S. Timashev, V. V. Firsov, and V. I. Yusupov, *Laser Phys. Lett.*, **7**, 401 (2010).
51. V. Aggarwal, L. F. Reichenbach, M. Enders, T. Muller, S. Wolff, M. Crone, M. Türk, and S. Bräse, *Chem.—Eur. J.*, **19**, 12794 (2013).
52. S. Wolff, M. Crone, T. Muller, M. Enders, S. Bräse, and M. Türk, *J. Supercrit. Fluids*, **95**, 588 (2014).
53. C. H. Yen, K. Shimizu, Y. Y. Lin, F. Bailey, I. F. Cheng, and C. M. Wai, *Energy & Fuels*, **21**, 2268 (2007).
54. A. Bayrakceken, B. Cangul, L. C. Zhang, M. Aindow, and C. Erkey, *Int. J. Hydrogen Energy*, **35**, 11669 (2010).
55. S. E. Bozbag, U. Unal, M. A. Kurykin, C. J. Ayala, M. Aindow, and C. Erkey, *J. Phys. Chem. C*, **117**, 6777 (2013).
56. C. F. Karanikas and J. J. Watkins, *Microelectron. Eng.*, **87**, 566 (2010).
57. J. M. Blackburn, D. P. Long, A. Cabanas, and J. J. Watkins, *Science*, **294**, 141 (2001).
58. E. Kondoh and J. Fukuda, *J. Supercrit. Fluids*, **44**, 466 (2008).
59. E. T. Hunde and J. J. Watkins, *Chem. Mater.*, **16**, 498 (2004).
60. H. O. Pierson, in *Handbook of Chemical Vapor Deposition (CVD) Principles, Technology, and Applications* (Noyes Publications, New York) (1999).
61. F. J. Maldonado-Hodar, M. A. Ferro-Garcia, J. Rivera-Utrilla, and C. Moreno-Castilla, *Carbon*, **37**, 1199 (1999).
62. E. Bekyarova and K. Kaneko, *Adv. Mater.*, **12**, 1625 (2000).
63. S. Martinez, A. Vallribera, C. L. Cotet, M. Popovici, L. Martin, A. Roig, M. Moreno-Manas, and E. Molins, *New J. Chem.*, **29**, 1342 (2005).
64. T. F. Baumann, G. A. Fox, J. H. Satcher, N. Yoshizawa, R. W. Fu, and M. S. Dresselhaus, *Langmuir*, **18**, 7073 (2002).
65. J. M. Miller, B. Dunn, T. D. Tran, and R. W. Pekala, *J. Electrochem. Soc.*, **144**, L309 (1997).
66. J. H. Jang, S. Han, T. Hyeon, and S. M. Oh, *J. Power Sources*, **123**, 79 (2003).
67. M. B. Dawidziuk, F. Carrasco-Marin, and C. Moreno-Castilla, *Carbon*, **47**, 2679 (2009).
68. Y. H. Lin, X. L. Cui, C. Yen, and C. M. Wai, *J. Phys. Chem. B*, **109**, 14410 (2005).
69. G. I. Garrido, F. C. Patcas, G. Upper, M. Tuerk, S. Yilmaz, and B. Kraushaar-Czarnezki, *Appl. Catal. A-Gen.*, **338**, 58 (2008).
70. S. G. Aspromonte, A. Sastre, A. V. Boix, M. J. Cocero, and E. Alonso, *Microporous Mesoporous Mater.*, **148**, 53 (2012).
71. J. Morere, S. Royuela, G. Asensio, P. Palomino, E. Enciso, C. Pando, and A. Cabanas, *Phil. Trans. R. Soc. A—Math. Phys. Eng. Sci.*, **373**, 16 (2015).
72. J. S. Wang, C. M. Wai, G. J. Brown, and S. D. Apt, *Langmuir*, **32**, 4635 (2016).
73. S. Wolff, M. Crone, T. Muller, M. Enders, S. Bräse, and M. Türk, *J. Supercrit. Fluids*, **95**, 588 (2014).
74. Y. Zhang, D. F. Kang, C. Saquing, M. Aindow, and C. Erkey, *Ind. Eng. Chem. Res.*, **44**, 4161 (2005).
75. U.S. Department of Energy, (2018), Cost Projections of PEM Fuel Cell Systems for Automobiles and Medium-Duty Vehicles Webinar, https://www.energy.gov/sites/prod/files/2018/04/f51/fcto_webinarslides_2018_costs_pem_fc_autos_trucks_042518.pdf.
76. X. R. Ye, Y. H. Lin, and C. M. Wai, *Chem. Commun.*, 642 (2003).
77. X. R. Ye, Y. H. Lin, C. M. Wang, M. H. Engelhard, Y. Wang, and C. M. Wai, *J. Mater. Chem.*, **14**, 908 (2004).
78. Y. H. Lin, X. L. Cui, and X. R. Ye, *Electrochem. Commun.*, **7**, 267 (2005).
79. G. Girishkumar, K. Vinodgopal, and P. V. Kamat, *J. Phys. Chem. B*, **108**, 19960 (2004).
80. J. Zhao, L. Q. Zhang, T. Chen, H. Yu, L. Zhang, H. Xue, and H. Q. Hu, *J. Phys. Chem. C*, **116**, 21374 (2012).
81. J. Zhao, Z. S. Liu, H. Q. Li, W. B. Hu, C. Z. Zhao, P. Zhao, and D. L. Shi, *Langmuir*, **31**, 2576 (2015).
82. J. Zhao, H. Yu, Z. S. Liu, M. Ji, L. Q. Zhang, and G. W. Sun, *J. Phys. Chem. C*, **118**, 1182 (2014).
83. B. Seger and P. V. Kamat, *J. Phys. Chem. C*, **113**, 7990 (2009).
84. C. Xu, X. Wang, and J. W. Zhu, *J. Phys. Chem. C*, **112**, 19841 (2008).
85. E. E. Said-Galiyev, A. Y. Nikolaev, E. E. Levin, E. K. Lavrentyeva, M. O. Gallyamov, S. N. Polyakov, G. A. Tsirlina, O. A. Petrii, and A. R. Khokhlov, *J. Solid State Electrochem.*, **15**, 623 (2011).
86. A. D. Taylor, R. C. Sekol, J. M. Kizuka, S. D'Cunha, and C. M. Comisar, *J. Catal.*, **259**, 5 (2008).
87. K. Shimizu, I. F. Cheng, J. S. Wang, C. H. Yen, B. Yoon, and C. M. Wai, *Energy & Fuels*, **22**, 2543 (2008).
88. A. Bayrakceken, A. Smirnova, U. Kitkamthorn, M. Aindow, L. Turker, I. Eroglu, and C. Erkey, *J. Power Sources*, **179**, 532 (2008).
89. A. Bayrakceken, A. Smirnova, U. Kitkamthorn, M. Aindow, L. Turker, I. Eroglu, and C. Erkey, *Chem. Eng. Commun.*, **196**, 194 (2009).
90. S. E. Bozbag, T. Gumusoglu, S. Yilmazturk, C. J. Ayala, M. Aindow, H. Deligoz, and C. Erkey, *J. Supercrit. Fluids*, **97**, 154 (2015).
91. S. B. Barim, A. Bayrakceken, S. E. Bozbag, L. C. Zhang, R. Kizilel, M. Aindow, and C. Erkey, *Microporous Mesoporous Mater.*, **245**, 94 (2017).
92. H. A. Gasteiger, S. S. Kocha, B. Sompalli, and F. T. Wagner, *Appl. Catal. B-Environ.*, **56**, 9 (2005).
93. M. H. Shao, A. Peles, and K. Shoemaker, *Nano Lett.*, **11**, 3714 (2011).
94. E. Antolini, *Appl. Catal. B-Environ.*, **88**, 1 (2009).
95. J. Marie, S. Berthon-Fabry, M. Chatenet, E. Chainet, R. Pirard, N. Cornet, and P. Achard, *J. Appl. Electrochem.*, **37**, 147 (2007).
96. A. Smirnova, X. Dong, H. Hara, A. Vasiliev, and N. Sammes, *Int. J. Hydrogen Energy*, **30**, 149 (2005).
97. N. Job, F. Maillard, J. Marie, S. Berthon-Fabry, J. P. Pirard, and M. Chatenet, *J. Mater. Sci.*, **44**, 6591 (2009).
98. V. Bock, A. Emmerling, and J. Fricke, *J. Non-Cryst. Solids*, **225**, 69 (1998).
99. F. J. Maldonado-Hodar, C. Moreno-Castilla, J. Rivera-Utrilla, Y. Hanzawa, and Y. Yamada, *Langmuir*, **16**, 4367 (2000).
100. K. Cheng, D. P. He, T. Peng, H. F. Lv, M. Pan, and S. C. Mu, *Electrochim. Acta*, **132**, 356 (2014).
101. Q. H. Huang, F. F. Tao, L. L. Zou, T. Yuan, Z. Q. Zou, H. F. Zhang, X. G. Zhang, and H. Yang, *Electrochim. Acta*, **152**, 140 (2015).
102. N. M. Markovic, H. A. Gasteiger, and P. N. Ross, *J. Phys. Chem.*, **99**, 3411 (1995).
103. S. Y. Ang and D. A. Walsh, *J. Power Sources*, **195**, 2557 (2010).
104. L. Quan, X. L. Yu, T. Wang, W. C. Yin, J. Q. Liu, L. Wang, and Y. H. Zhang, *Appl. Surf. Sci.*, **494**, 691 (2019).
105. Y. Y. Liang, H. L. Wang, J. G. Zhou, Y. G. Li, J. Wang, T. Regier, and H. J. Dai, *JACS*, **134**, 3517 (2012).
106. P. Q. Yin et al., *Angew. Chem. Int. Ed.*, **55**, 10800 (2016).
107. W. J. Jiang, L. Gu, L. Li, Y. Zhang, X. Zhang, L. J. Zhang, J. Q. Wang, J. S. Hu, Z. D. Wei, and L. J. Wan, *JACS*, **138**, 3570 (2016).
108. H. L. Peng, Z. Y. Mo, S. J. Liao, H. G. Liang, L. J. Yang, F. Luo, H. Y. Song, Y. L. Zhong, and B. Q. Zhang, *Sci. Rep.*, **3**, 7 (2013).
109. C. L. Lai, P. Kolla, Y. Zhao, H. Fong, and A. L. Smirnova, *Electrochim. Acta*, **130**, 431 (2014).
110. S. Unsal, M. B. Yagci, S. E. Bozbag, B. Deljoo, M. Aindow, and C. Erkey, *Energy Technol.*, **7**, 1900450 (2019).
111. Z. Chen, J. F. Lu, Y. J. Ai, Y. F. Ji, T. Adschiri, and L. J. Wan, *ACS Appl. Mater. Interfaces*, **8**, 35132 (2016).
112. P. Thangasamy, A. Ramesh, and M. Sathish, *ChemistrySelect*, **2**, 5978 (2017).
113. X. X. Lin, A. J. Wang, K. M. Fang, J. H. Yuan, and J. J. Feng, *ACS Sustain. Chem. Eng.*, **5**, 8675 (2017).
114. H. F. Lv et al., *JACS*, **137**, 5859 (2015).
115. Y. Shi, J. Wang, C. Wang, T. T. Zhai, W. J. Bao, J. J. Xu, X. H. Xia, and H. Y. Chen, *JACS*, **137**, 7365 (2015).
116. G. D. Li and Z. Y. Tang, *Nanoscale*, **6**, 3995 (2014).
117. T. R. Karl and K. E. Trenberth, *Science*, **302**, 1719 (2003).

118. R. a. D. A. Ussiri, in *Carbon Sequestration for Climate Change Mitigation and Adaptation* (Springer, Cham, Switzerland) (2017).
119. M. De Falco, M. Capocelli, and G. Centi, *Chem. Eng. J.*, **294**, 400 (2016).
120. G. L. Zhou, H. R. Liu, K. K. Cui, A. P. Jia, G. S. Hu, Z. J. Jiao, Y. Q. Liu, and X. M. Zhang, *Appl. Surf. Sci.*, **383**, 248 (2016).
121. H. Muroyama, Y. Tsuda, T. Asakoshi, H. Masitah, T. Okanishi, T. Matsui, and K. Eguchi, *J. Catal.*, **343**, 178 (2016).
122. C. Fukuhara, K. Hayakawa, Y. Suzuki, W. Kawasaki, and R. Watanabe, *Appl. Catal. A-Gen.*, **532**, 12 (2017).
123. C. Genovese, C. Ampelli, S. Perathoner, and G. Centi, *J. Catal.*, **308**, 237 (2013).
124. C. Ampelli, C. Genovese, M. Errahali, G. Gatti, L. Marchese, S. Perathoner, and G. Centi, *J. Appl. Electrochem.*, **45**, 701 (2015).
125. A. Del Castillo, M. Alvarez-Guerra, and A. Irabien, *AIChE J.*, **60**, 3557 (2014).
126. Q. N. Wang, H. Dong, and H. B. Yu, *J. Power Sources*, **271**, 278 (2014).
127. H. R. Jhong, F. R. Brushett, and P. J. A. Kenis, *Adv. Energy Mater.*, **3**, 589 (2013).
128. J. Medina-Ramos, R. C. Pupillo, T. P. Keane, J. L. DiMeglio, and J. Rosenthal, *J. Am. Chem. Soc.*, **137**, 5021 (2015).
129. Z. Bitar, A. Fecant, E. Trela-Baudot, S. Chardon-Noblat, and D. Pasquier, *Appl. Catal. B-Environ.*, **189**, 172 (2016).
130. J. L. Yu, H. Y. Liu, S. Q. Song, Y. Wang, and P. Tsiakaras, *Appl. Catal. A-Gen.*, **545**, 159 (2017).
131. M. T. Mehran, S. B. Yu, D. Y. Lee, J. E. Hong, S. B. Lee, S. J. Park, R. H. Song, and T. H. Lim, *Appl. Energy*, **212**, 759 (2018).
132. C. Jimenez, J. Garcia, R. Camarillo, F. Martinez, and J. Rincon, *Energy & Fuels*, **31**, 3038 (2017).
133. J. Garcia, C. Jimenez, F. Martinez, R. Camarillo, and J. Rincon, *J. Catal.*, **367**, 72 (2018).
134. M. Le, M. Ren, Z. Zhang, P. T. Sprunger, R. L. Kurtz, and J. C. Flake, *J. Electrochem. Soc.*, **158**, E45 (2011).
135. J. Albo and A. Irabien, *J. Catal.*, **343**, 232 (2016).
136. R. Passalacqua, S. Parathoner, G. Centi, A. Halder, E. C. Tyo, B. Yang, S. Seifert, and S. Vajda, *Catal. Sci. Technol.*, **6**, 6977 (2016).
137. S. T. Ahn, I. Abu-Baker, and G. T. R. Palmore, *Catal. Today*, **288**, 24 (2017).
138. S. E. Bozbag, S. O. Kostenko, M. A. Kurykin, V. N. Khrustalev, A. R. Khokhlov, L. Zhang, M. Aindow, and C. Erkey, *J. Nanopart. Res.*, **14**, 973 (2012).
139. L. Y. Wang, L. H. Zhuo, C. Zhang, and F. Y. Zhao, *Chem.—Eur. J.*, **20**, 4308 (2014).
140. J. P. Bosco, M. P. Humbert, and J. G. Chen, in *Design of Heterogeneous Catalysts New Approaches based on Synthesis, Characterization and Modeling*, ed. U. S. Ozkan (Wiley-VCH, Weinheim) p. 195 (2009).
141. J. R. Kitchin, J. K. Nørskov, M. A. Barteau, and J. G. Chen, *Phys. Rev. Lett.*, **93**, 156801 (2004).
142. A. Winkler, D. Ferri, and R. Hauert, *Catal. Today*, **155**, 140 (2010).
143. M. H. Wiebenga, C. H. Kim, S. J. Schmieg, S. H. Oh, D. B. Brown, D. H. Kim, J.-H. Lee, and C. H. F. Peden, *Catal. Today*, **184**, 197 (2012).
144. S. Koh and P. Strasser, *JACS*, **129**, 12624 (2007).
145. J. Greeley and J. K. Nørskov, *Surf. Sci.*, **592**, 104 (2005).
146. V. R. Stamenkovic, B. Fowler, B. S. Mun, G. Wang, P. N. Ross, C. A. Lucas, and N. M. Marković, *Science*, **315**, 493 (2007).
147. P. Mani, R. Srivastava, and P. Strasser, *J. Phys. Chem. C*, **112**, 2770 (2008).
148. Y. Lin, X. C. H. Yen, and C. M. Wai, *Langmuir*, **21**, 11474 (2005).
149. M. Watanabe, Y. M. Zhu, H. Igarashi, and H. Uchida, *Electrochem. Commun.*, **68**, 244 (2000).
150. C. H. Yen, K. Shimizu, Y.-Y. Lin, F. Bailey, I. F. Cheng, and C. M. Wai, *Energy & Fuels*, **21**, 2268 (2007).
151. G. An, P. Yu, L. Mao, Z. Sun, Z. Liu, S. Miao, Z. Miao, and K. Ding, *Carbon*, **45**, 536 (2007).
152. A. Bayrakceken, B. Cangül, L. C. Zhang, M. Aindow, and C. Erkey, *Int. J. Hydrogen Energy*, **35**, 11669 (2010).
153. S. B. Barim, S. E. Bozbag, H. Yu, R. Kızılel, M. Aindow, and C. Erkey, *Catal. Today*, **310**, 166 (2018).
154. S. Koh, N. Hahn, C. F. Yu, and P. Strasser, *J. Electrochem. Soc.*, **155**, B1281 (2008).
155. M. Oezaslan, F. Hasche, and P. Strasser, *J. Electrochem. Soc.*, **159**, B444 (2012).
156. S. B. Barim, S. E. Bozbag, B. Deljoo, M. Aindow, and C. Erkey, *Fuel Cells* (2020), at press.
157. Y. Z. Zhou, X. N. Cheng, C. H. Yen, C. M. Wai, C. M. Wang, J. Yang, and Y. H. Lin, *J. Power Sources*, **347**, 69 (2017).
158. E. Reverchon and R. Adami, *J. Supercrit. Fluids*, **37**, 1 (2006).
159. J. J. Watkins and T. J. McCarthy, *Chem. Mater.*, **7**, 1991 (1995).
160. A. R. Berens and G. S. Huvard, in *Supercritical Fluid Science and Technology* (American Chemical Society, Washington, DC) 406, p. 207 (1989).
161. D. L. Tomasko, H. Li, D. Liu, X. Han, M. J. Wingert, L. J. Lee, and K. W. Koelling, *Ind. Eng. Chem. Res.*, **42**, 6431 (2003).
162. E. J. Beckman, *J. Supercrit. Fluids*, **28**, 121 (2004).
163. S. G. Kazarian, N. H. Brantley, B. L. West, M. F. Vincent, and C. A. Eckert, *Appl. Spectrosc.*, **51**, 491 (1997).
164. J. von Schnitzler and R. Eggers, *J. Supercrit. Fluids*, **16**, 81 (1999).
165. M. Ge, S. E. Bozbag, C. J. Ayala, M. Aindow, and C. Erkey, *Mater. Chem. Phys.*, **180**, 1 (2016).
166. R. C. Jiang, Y. Zhang, S. Swier, X. Z. Wei, C. Erkey, H. R. Kunz, and J. M. Fenton, *Electrochem. Solid State Lett.*, **8**, A611 (2005).
167. Y. Zhang and C. Erkey, *Ind. Eng. Chem. Res.*, **44**, 5312 (2005).
168. D. Kim, J. Sauk, J. Byun, K. S. Lee, and H. Kim, *Solid State Ionics*, **178**, 865 (2007).
169. J. J. Watkins, J. M. Blackburn, and T. J. McCarthy, *Chem. Mater.*, **11**, 213 (1999).
170. J. M. Blackburn, D. P. Long, and J. J. Watkins, *Chem. Mater.*, **12**, 2625 (2000).
171. M. Majimel, S. Marre, E. Garrido, and C. Aymonier, *Chem. Vap. Deposition*, **17**, 342 (2011).
172. O. Pascu, S. Marre, and C. Aymonier, *Nanotechnol. Rev.*, **4**, 487 (2015).
173. A. H. Romang and J. J. Watkins, *Chem. Rev.*, **110**, 459 (2010).
174. A. O'Neil and J. J. Watkins, *MRS Bull.*, **30**, 967 (2005).
175. J. M. Bassat, C. Mesguich, C. Ferchaud, Y. Zhang-Steenwinkel, F. van Berkel, C. Aymonier, J. J. Watkins, and J. C. Grenier, *ECS Trans.*, **35**, 1945 (2011).
176. D. Mesguich, C. Aymonier, J. M. Bassat, F. Mauvy, E. You, and J. J. Watkins, *Chem. Mater.*, **23**, 5323 (2011).
177. Q. Le Trequesser, D. Mesguich, E. You, C. Aymonier, and J. J. Watkins, *J. Supercrit. Fluids*, **66**, 328 (2012).
178. Q. H. Do, C. C. Zeng, C. Zhang, B. Wang, and J. Zheng, *Nanotechnology*, **22**, 365402 (2011).
179. Q. H. Do and C. C. Zeng, *Ind. Eng. Chem. Res.*, **57**, 6863 (2018).